Activity-dependent spinal cord neuromodulation rapidly restores trunk and leg motor functions after complete paralysis

Rowald, Andreas; Komi, Salif; Demesmaeker, Robin; Baaklini, Edeny; Hernandez-Charpak, Sergio Daniel; Paoles, Edoardo; Montanaro, Hazael; Cassara, Antonino; Becce, Fabio; Lloyd, Bryn; Newton, Taylor; Ravier, Jimmy; Kinany, Nawal; D’Ercole, Marina [**and 55 more**]

How to cite

ROWALD, Andreas et al. Activity-dependent spinal cord neuromodulation rapidly restores trunk and leg motor functions after complete paralysis. In: Nature medicine, 2022, vol. 28, n° 2, p. 260–271. doi: 10.1038/s41591-021-01663-5

This publication URL: https://archive-ouverte.unige.ch/unige:168804
Publication DOI: 10.1038/s41591-021-01663-5

Title

Activity-dependent spinal cord neuromodulation rapidly restores trunk and leg motor functions after complete paralysis

Author list

Andreas Rowald[1,2,3,27], Salif Komi[1,2,3,27], Robin Demesmaeker[1,2,3,27] , Edeny Baaklini[1,2,3], Sergio Daniel Hernandez-Charpak[1,2,3], Edoardo Paoles[4], Hazael Montanaro[8,9], Antonino Cassara[8], Fabio Becce[6], Bryn Lloyd[8], Taylor Newton[8], Jimmy Ravier[1,2,3], Nawal Kinany[1,19,22,5], Marina D´Ercole[4], Aurélie Paley[2,3], Nicolas Hankov[1,2,3], Camille Varescon[1,2,3], Laura McCracken[1,2,3], Molywan Vat[2,3], Miroslav Caban[4,5], Anne Watrin[4], Charlotte Jacquet[4], Léa Bole-Feysot[1,2,3], Cathal Harte[1,2,3], Henri Lorach[1,2,3], Andrea Galvez[1,2,3], Manon Tschopp[2], Natacha Herrmann[2], Moïra Wacker[2], Lionel Geernaert[2], Isabelle Fodor[2], Valentin Radevich[2], Katrien Van Den Keybus[2], Grégoire Eberle[2], Etienne Pralong[10], Maxime Roulet[3,10], Jean-Baptiste Ledoux[6,7], Eleonora Fornari[6,7], Stefano Mandija[17], Loan Mattera[11], Roberto Martuzzi[11], Bruno Nazarian[12], Stefan Benkler[10], Simone Callegari[16], Nathan Greiner[1,2,3], Benjamin Fuhrer[1,2], Martijn Froeling[17], Nik Buse[18], Tim Denison[14,18], Rik Buschman[18], Christian Wende[19], Damien Ganty[4], Jurriaan Bakker[4], Vincent Delattre[4], Hendrik Lambert[4], Karen Minassian[20], Cornelis A T van den Berg[17], Anne Kavounoudias[13], Silvestro Micera[,21,22], Dimitri Van De Ville[5,23], Quentin Barraud[1,2,3], Erkan Kurt[15], Niels Kuster[8,9,16], Esra Neufeld[8,9,16], Marco Capogrosso[1,24,25], Leonie Asboth[1,2,3], Fabien B. Wagner[1,2,3,26,28] and Jocelyne Bloch[1,2,3,10,28,✉] & Grégoire Courtine[1,2,3,10,28,✉]

Affiliations

1. Center for Neuroprosthetics and Brain Mind Institute, School of Life Sciences, Swiss Federal Institute of Technology (EPFL), Lausanne, Switzerland
2. Department of Clinical Neuroscience, Lausanne University Hospital (CHUV) and University of Lausanne (UNIL), Lausanne, Switzerland
3. Defitech Center for Interventional Neurotherapies (NeuroRestore), EPFL/CHUV/UNIL, Lausanne, Switzerland
4. ONWARD medical, Lausanne, Switzerland
5. Institute of Bioengineering, Swiss Federal Institute of Technology (EPFL), a Lausanne, Switzerland
6. Department of Diagnostic and Interventional Radiology, Lausanne University Hospital (CHUV) and University of Lausanne (UNIL), Lausanne, Switzerland
7. Biomedical Imaging Center (CIBM), CHUV-MR section, Lausanne Switzerland
8. Foundation for Research on Information Technologies in Society (IT'IS), Zurich, Switzerland

9. Department for Information Technology and Electrical Engineering, Swiss Federal Institute of Technology (ETHZ), Zurich, Switzerland
10. Department of Neurosurgery, Lausanne University Hospital (CHUV), Lausanne
11. Fondation Campus Biotech Genève, 1202, Geneva, Switzerland
12. Aix-Marseille Univ, CNRS, Institut des Neurosciences de la Timone, INT UMR 7289, Marseille, France
13. Aix-Marseille Univ, CNRS, Laboratoire de Neurosciences Cognitives, LNC UMR 7291, Marseille, France
14. Department of Engineering Science, University of Oxford, Oxford, United Kingdom
15. Radboud University Medical Center Nijmegen, University of Neurosurgery, Nijmegen, Netherlands
16. ZMT ZurichMedTech, Zurich, Switzerland
17. University Medical Center Utrecht, Utrecht, Netherlands
18. Medtronic, Minneapolis, MN, USA
19. Technical University of Munich (TUM), Chair of Medical Materials and Implants, Munich, Germany
20. Center for Medical Physics and Biomedical Engineering, Medical University of Vienna, Austria
21. Bertarelli Foundation Chair in Translational Neuroengineering, Center for Neuroprosthetics and Institute of Bioengineering, School of Bioengineering, EPFL, Lausanne, Switzerland
22. The BioRobotics Institute, Scuola Superiore Sant'Anna, Pisa, Italy
23. Department of Radiology and Medical Informatics, University of Geneva (UNIGE), Geneva, Switzerland
24. Department of Neuroscience and Movement Science, University of Fribourg, Fribourg, Switzerland
25. Department of Neurological Surgery, University of Pittsburgh, Pittsburgh, USA
26. Institut des Maladies Neurodégénératives (CNRS UMR 5293), Université de Bordeaux, France
27. These authors contributed equally: Andreas Rowald, Salif Komi, Robin Demesmaeker
28. These authors jointly supervised this work: Fabien Wagner, Jocelyne Bloch, Gregoire Courtine

✉ email:

jocelyne.bloch@chuv.ch (ORCID: 0000-0002-6405-1590)

gregoire.courtine@epfl.ch (ORCID: 0000-0002-5744-4142)

Abstract

Epidural electrical stimulation (EES) targeting the dorsal roots of lumbosacral segments restored walking in people with spinal cord injury (SCI). However, EES was delivered with multielectrode paddle leads that were originally designed to target the dorsal column of the spinal cord. Here, we hypothesized that an arrangement of electrodes targeting the ensemble of dorsal roots involved in leg and trunk movements would result in superior efficacy, restoring more diverse motor activities after the most severe SCI. To test this hypothesis, we established a computational framework that informed the optimal arrangement of electrodes on a new paddle lead and guided its neurosurgical positioning. We also developed a software supporting the rapid configuration of activity-specific stimulation programs that reproduced the natural activation of motor neurons underlying each activity. We tested these neurotechnologies in three individuals with complete sensorimotor paralysis, as part of an ongoing clinical trial (clinicaltrials.gov, NCT02936453). Within a single day, activity-specific stimulation programs enabled the three individuals to stand, walk, cycle, swim, and control trunk movements. Neurorehabilitation mediated sufficient improvement to restore these activities in community settings, opening a realistic path to support everyday mobility with EES in people with SCI.

Short summary

Purposed-built technologies for spatiotemporal stimulation of the spinal cord restore standing, walking, cycling, swimming and trunk control in people with complete paralysis due to a spinal cord injury

Main text

Three decades of preclinical[1–6] and clinical[7–16] research showed that EES applied over the lumbosacral spinal cord can restore walking after SCI. A subset of the treated individuals with motor complete paralysis could even walk overground with EES after many months of intense training assisted by multiple physical therapists[7,10]. However, translating these isolated proofs of concept into a commonly available therapy requires neurotechnologies that not only enable the rapid recovery of numerous motor activities with limited human resources, but also mediate this recovery in every treated individual. Here, we aim to address these challenges.

EES recruits large-diameter afferent fibers at their entrance in the spinal cord through the dorsal roots[12,17–20]. The recruitment of these fibers leads to the activation of motor neurons embedded in the spinal segment innervated by the root wherein these fibers reside[4,8]. Therefore, targeting individual dorsal roots enable the modulation of specific motor neuron ensembles[4,8,21]. This biological principle guided the development of EES programs[4,21–23] that target the individual dorsal roots with a predefined timing to reproduce the natural spatiotemporal activation pattern[24,25] of motor neurons during walking. Compared to continuous EES, these biomimetic stimulation programs have mediated superior recovery of walking after SCI[4,8,12,21].

EES has been delivered using repurposed neurotechnologies that were initially designed to alleviate pain[7–14]. These neurotechnologies include paddle leads with an arrangement of electrodes that target the dorsal column[26]. Instead, the recovery of motor functions requires targeting the dorsal roots[27]. Moreover, the short length of existing paddle leads limits the number of dorsal roots that can be targeted with EES. Therefore, current neurotechnologies fail to leverage the biological principles through which EES restores movement after SCI.

Here, we designed and fabricated a new paddle lead with an arrangement of electrodes that targeted the ensemble of dorsal roots involved in leg and lower-trunk movements. We also established a computational framework combining high-resolution structural and functional imaging to optimize the surgical placement of this lead. Finally, we developed a software to support the rapid configuration of biomimetic stimulation programs.

We aimed to leverage this portfolio of purposed-built neurotechnologies to elaborate activity-dependent biomimetic stimulation programs that address the deficits of individuals presenting with the most severe forms of SCI across a broad range of activities, including the critically-important control of the trunk [10,28,29].

Results

Variability of spinal cord topology

Sacral (S1-S2), lumbar (L1-L5) and low-thoracic (T12) dorsal roots project to spinal segments containing motor neurons innervating leg and lower-trunk muscles (**Fig. 1a**). Therefore, we aimed to identify an arrangement of electrodes that would be suitable to target all of these roots across the human population. We first asked whether the inter-individual variability of spinal cord anatomy would be compatible with this aim.

Neuroanatomical quantification of 27 spinal cords exposed a pronounced variability of spinal segment lengths, in particular across upper lumbar segments (**Fig. 1b**). We complemented this survey with an analysis of the tridimensional topology of dorsal roots, since we showed that this topology determines the distribution of EES-induced electric potentials along the roots[30]. To enable this visualization, we optimized structural magnetic resonance imaging (MRI) sequences that increased the tridimensional spatial resolution while enhancing the contrast resolution between the cerebrospinal fluid and spinal cord tissues (**Fig. 1c** and **Extended Data Fig. 1**). This contrast enabled the semi-automated conversion of MRI and computerized tomography (CT) images into realistic anatomical models of the entire spine (**Fig. 1d**). This visualization confirmed the pronounced variability in the rostrocaudal distribution of dorsal roots (**Fig. 1b**). Instead, we found that the widths of the dorsal root entry zones were remarkably consistent (**Fig. 1b** and **Extended Data Fig. 2**).

Atlas of spinal cord models

Our pulse generator could accommodate 16 electrodes. Therefore, our challenge was to identify an arrangement of 16 electrodes that accessed the 16 targeted dorsal roots despite the variable topology of the spinal cord. We posited that resolving this challenge would require tradeoffs, and that identifying these tradeoffs would be contingent on computational models.

We thus established a pipeline to generate highly-realistic computational models of the interactions between EES and the spinal cord. This pipeline leverages the verified anatomical and biophysical models of the *Sim4Life* computational life-sciences simulation platform[31] to generate tridimensional finite element models of the spine from CT and MRI scans (**Fig. 1** and **Extended Data Fig. 1**), creates models of rootlet bundles and their innervation patterns (**Extended Data Fig. 2**), and functionalized these geometries with fiber models covering the entire populations of efferent and afferent fibers (**Fig. 1f**). The physics and neuron electrophysiology solvers of the *Sim4Life* simulation platform then predicted the probability of recruiting these fibers when delivering EES. These simulations confirmed[19] that EES preferentially recruit large-diameter afferents, since Aa fibers were nearly all recruited before the depolarisation of Ab fibers (**Fig. 1g**).

We then used this pipeline to generate a freely available atlas of 15 personalized computational models (HTML link) that provided a resource to study the optimal arrangements of electrode across a large human population.

Optimized electrode arrangement

We reasoned that identifying an optimal arrangement of electrodes would require circumscribing the analysis to the key features that determine the selectivity of EES. We thus focused our analysis on four features (**Fig. 2a**):

(i) Rostrocaudal distributions: we merged all the spinal cords of the atlas into a unified model that captured the average topology of the human spinal cord. This model informed the optimal length of the paddle. We then distributed the electrodes uniformly along the rostrocaudal direction (**Fig. 2b**).

(ii) Lateral positions to maximize left-right selectivity: simulations predicted a maximal selectivity with an electrode positioned 2.3 mm lateral to the midline. However, this selectivity declined by 50% with a lateral shift as small as 1 mm. Such deviations are inevitable when a paddle lead is inserted into the irregular spinal canal. Simulations indicated that placing the electrodes at 4.7 mm from the midline would mitigate the impact of potential mediolateral deviations (**Fig. 2c**).

(iii) Midline positions to steer current: simulations showed that increasing the amplitude of EES leads to a proportional recruitment of non-targeted dorsal roots, especially from the contralateral side (**Fig. 2d**). To minimize this undesired recruitment, we incorporated midline electrodes, since simulations revealed that creating multipolar configurations with lateral and midline electrodes steered the current toward the targeted root while minimizing the recruitment of contralateral roots (**Fig. 2d**).

(iv) Arrangement for the sacral region: the agglutination of the lumbar rootlets around sacral segments is an impediment to the selective recruitment of the sacral root entry zones (**Fig. 2e**). Since the somatotopy of the lumbar dorsal rootlet bundles is maintained along the transverse axis of sacral segments, we reasoned that a transverse arrangement of electrodes would rescue this selectivity. Simulations confirmed these considerations (**Fig. 2e**).

We translated these predictions into an arrangement of 16 electrodes that we accommodated on a new paddle lead fabricated with standard medical-grade processes (**Fig. 2f**).

Precise preoperative planning

We then evaluated the selectivity of this lead across the 15 computational models. Performances differed widely across individual models (**Extended Data Fig. 2**), as expected from the mismatch between a fixed arrangement of electrodes and the large variability of spinal cord topology. We concluded that a preoperative planning was essential to optimize the positioning of the lead (**Supplementary Data Table 1**).

We first generated a personalized model of the spine for each participant (**Fig. 3a**). Since EES modulates motor neurons through the recruitment of large-diameter afferents, we presumed that localizing the predominant projectome of these afferents would improve the models, and thus the accuracy of simulations.

To expose this projectome, we monitored the blood oxygenation level dependent (BOLD) response in the spinal cord[32] when activating proprioceptors, which are innervated by large-diameter afferents. We employed two methods (**Extended Data Fig. 3)**. First, we mobilized each joint passively to elicit a proprioceptive message from the lengthened muscles. Second, we implemented a more precise method based on the application of a mechanical vibration to the tendon[33,34]. Muscle tendon vibration recruits muscle spindle afferents embedded in the muscle attached to the vibrated tendon[35].

While proprioceptive afferents project across several segments, the recruitment of these afferents leads to the predominant activation of homonymous motor neurons[36]. Accordingly, the recruitment of proprioceptive afferents from muscles distributed at the ankle, knee and hip levels induced BOLD responses that remained confined within one or two segments (**Extended Data Fig. 3)**. These responses exposed the predominant projectome of large-diameter afferents innervating the mobilized muscle. We integrated the projectome from key leg muscles into the personalized computational models (**Extended Data Fig. 4)**.

To determine the optimal rostrocaudal position of the paddle lead, we implemented an algorithm that calculated the relative activation of the targeted muscles with respect to the non-targeted muscles[8] (**Extended Data Fig. 4** and **Supplementary Video 1**).

Intraoperative validation of model predictions

We next aimed to validate the predictions of simulations, and the relevance of improving the precision of the models with personalized features to generate these predictions. We conducted intraoperative experiments in 3 participants of the ongoing clinical trial STIMO (**Supplementary Data Table 1** and **Supplementary Video 1**).

We first performed an intraoperative tridimensional CT scan to map the predicted position of the lead to the anatomy of each participant, and thus guide its insertion. Once the lead was advanced at the predicted position, we quantified the selectivity of the electrodes located at each corner of the lead. We delivered single-pulses of EES to elicit muscle responses that we monitored with electromyographic recordings. We quantified the selectivity of each electrode using the same algorithm as in simulations.

We then studied whether alternative locations would permit superior selectivity. Moving the lead by approximately 2 mm in the rostral or caudal directions resulted in lower selectivity, indicating that the predicted position achieved the highest performance (**Fig. 3b**).

We finally asked whether the personalized features of the models were important for predicting the optimal position of the lead[37]. Simulations based on a generic computational model or theoretical myotome distributions failed to reach the same accuracy as personalized models (**Extended Data Fig. 5**).

Superior selectivity of the new electrode arrangement

We then aimed to demonstrate that the new arrangement of electrodes enhanced the coverage and selectivity of EES compared to leads originally designed for pain treatment. We selected the Specify 5-6-5, since this lead has been the most commonly used to restore walking in humans with SCI[7–10].

To enable a direct comparison, we performed an intraoperative assessment of the Specify 5-6-5 in the same participants. The length of the Specify 5-6-5 is shorter than the new lead by 18.8 mm. Accordingly, simulations predicted that the Specify 5-6-5 would not be able to target all the dorsal roots in these participants. Intraoperative electrophysiological quantifications confirmed these predictions (**Fig. 3c** and **Extended Data Fig. 4**).

Finally, we asked whether the transverse arrangement of electrodes at the bottom of the lead enabled a more selective recruitment of dorsal roots agglutinated in the thecal sac. We found that multipolar combinations of these electrodes enhanced the selective recruitment of triceps muscles, whose motor neurons are located in sacral segments (**Fig. 3d**).

Neurostimulation platform

Biomimetic EES requires the delivery of concurrent stimulation waveforms that are turned on and off with a precise timing[4,8,12,21]. Moreover, many activities necessitate adjustment of stimulation parameters in closed-loop via wireless links. To support these features, we upgraded the ACTIVA-RC implantable pulse generator with wireless communication modules (**Supplementary Fig. 1**). This neurostimulation platform supported real-time updates of EES frequency, amplitude and timing from up to 10 stimulation waveforms[8]. The new paddle lead was interfaced with the ACTIVA-RC, which was implanted in the abdomen.

We also developed a new software operating through touch-screen interfaces to enable the rapid configuration of activity-dependent stimulation programs (**Fig. 4**). To simplify these configurations, wireless recordings of kinematics and muscle activity are displayed in real-time, concomitantly to EES waveforms (**Supplementary Fig. 1** and **Supplementary Video 2**).

Immediate recovery of walking after complete paralysis

Our next objective was to demonstrate the superior performance of the new lead to restore walking after SCI. Previous studies showed that a subset of individuals with complete motor paralysis could step with EES following many months of training[7,10]. Here, we aimed to restore independent stepping on the first day of stimulation in all the participants.

We first assembled preoperative and intraoperative information into a library of cathode and anode configurations targeting the individual dorsal roots (**Extended data Fig. 6**). Each configuration aimed to modulate a specific ensemble of motor neurons that are confined within circumscribed regions of the spinal cord, termed motor hotspots (**Fig. 4b**). Each configuration was then optimized based on the responses elicited by EES. For this purpose, brief trains (500 ms) of stimulation were delivered in a supine position, since bursts elicited ample leg movements that identified potential undesired movements and thus facilitated the fine-tuning of anode-cathode combinations (**Extended data Fig. 6** and **Supplementary Video 2)**. Pulse frequencies were adjusted for extensor (20 Hz) versus flexor (100 Hz) muscles, since the motor neurons innervating these muscles exhibit distinct preferential activation frequencies[8] (**Extended data Fig. 7**). Elaborating this library did not last longer than one hour.

Once the library was configured, the temporal sequence of EES pulses was optimized for each participant. Walking involves stereotypical spatiotemporal patterns of motor hotspot activation that reflect changes in body mechanics[24,25] (**Fig. 4a,b**). Therefore, the next step consisted of injecting the electrode configurations targeting each motor hotspot into pre-established sequences of EES pulses that reproduce the natural pattern of motor hotspot activation during walking[4,8,21,38] (**Fig. 4b**). Finally, EES parameters were fine-tuned through a stimulation scheduler displayed on the software. This fine-tuning involved interactions with the physical therapist and participant who was attempting to walk (**Fig. 4c**). This procedure allowed the configuration of EES programs for walking within one hour.

All three participants exhibited complete sensorimotor paralysis (**Supplementary Table 1**). They were unable to take any step, and muscles remain quiescent during these attempts (**Extended data Fig. 8**). On the first day, all three participants could step independently on a treadmill, although gait patterns exhibited poor extension components. Consequently, substantial amounts of body weight support were necessary (**Fig. 4d**). After one to three additional days, gait patterns were sufficiently optimized to enable the three participants to ambulate independently overground while supported in a multidirectional body weight support system[39] (**Fig. 4e** and **Supplementary Video 2**). This recovery involved the production of substantial activity in leg muscles that coincided with pronounced excursions of hip, knee and ankle joints (**Fig. 4b** and **Extended data Fig. 8**).

Two out of the three participants could modulate the amplitude of leg movements when asked to increase their step length voluntarily (**Extended data Fig. 8**). Contrary to the fatigue that rapidly occurs with direct neuromuscular stimulation [40], the participants could produce up to 300 independent steps as early as the first day of stimulation (**Extended data Fig. 8**).

Extension to other motor activities

We reasoned that the principles through which EES restores walking could support the configuration of EES programs to enable other motor activities.

To test this possibility, we configured activity-specific stimulation programs that enabled the 3 participants to use their legs to swim in the water or pedal actively on a motorized bike (**Fig. 4f** and **Supplementary Video 3**). EES programs also supported rehabilitation exercises such as squats or leg press (**Fig. 4f** and **Supplementary Video 3**).

We applied the same principles to target trunk muscles (**Extended data Fig. 9**). Indeed, the participants showed impairments in the control of trunk postures (**Extended data Fig. 10**). EES programs targeting trunk muscles normalized trunk postures (**Fig.5a**) and improved the control of trunk movements. For example, participants who exhibited difficulties to regain an upright trunk posture from a flexed position performed this task with ease, as captured in the marked increase in the speed of these executions (**Fig. 5b** and **Supplementary Video 3**).

Recovery of independence in ecological settings

Activity-dependent stimulation programs enabled the immediate recovery of trunk and leg motor functions in people with complete paralysis. While weight bearing capacities and overall performances remain limited at this stage, this recovery provided the opportunity to engage the neuromuscular system into sustained and active training sessions. We thus asked whether performance would improve with practice, and whether these improvements would be sufficient to regain some independence in ecological settings.

The three participants underwent a 5-month neurorehabilitation program during which EES enabled them to stand, walk and perform a broad range of exercises 4 to 5 times per week. We developed a simplified software interface that allowed participants and physical therapists to switch between activity-dependent stimulation programs and to fine-tune key parameters of these programs. We also equipped the assistive devices with ergonomic clickers that trigger EES programs upon desire. For example, they could switch between standing and walking, or between the swing and stance phases of gait (**Supplementary Fig. 1**). Participants could select EES sequences that were executed in open-loop or triggered with clickers, or closed-loop control of these sequences based on wearable sensors (**Supplementary Fig. 1**).

Performance improved dramatically. All three participants progressively regained full-weight bearing capacities (**Fig. 6b**), which translated into the ability to stand independently in community settings (**Supplementary Video 4**). Improvement of gait patterns and weight bearing capacities allowed them to walk independently with the help of a front-wheel walker for stability, which enabled the performance of the 10-meter and 6 min walk test without any assistance (**Fig. 6c** and **Supplementary Video 2).** One of the participants even regained the ability to climb a staircase and to progress over complex terrains (**Supplementary Video 3**). Participants could also ride a recumbent trike powered with the arms and legs (**Fig. 6**). Finally, improved control of trunk postures allowed the practice of leisure activities such as boxing, enjoying a drink while standing at a bar, or paddling a canoe on a lake (**Fig. 6** and **Supplementary Video 3**).

These improvements coincided with a substantial increase in the mass of leg and trunk muscles (**Fig. 6c**). Moreover, two of the participants recovered the ability to activate proximal muscles voluntarily without EES (**Supplementary Fig. 2**).

Discussion

Here, we show that biomimetic EES enabled the recovery of standing, walking, cycling, swimming and trunk control within one day in three individuals with chronic complete paralysis.

After neurorehabilitation, the three treated individuals were able to leverage biomimetic EES to perform these activities in the community. Central to this radically increased efficacy compared to previous studies[7,10] was an arrangement of electrodes that targeted the ensemble of sacral, lumbar and low-thoracic dorsal roots involved in the production of leg and trunk movements, combined with a software that renders the configuration of activity-dependent stimulation programs rapid, simple and predictable.

While the three participants could ambulate independently, it is important to point out that they did not regain natural movements. Yet, this recovery was sufficient to perform various activities for extensive periods of time. Moreover, two participants were able to modulate leg movements during EES, suggesting that the stimulation boosted signals from residual descending pathways. The recovery of volitional muscle activation without EES following neurorehabilitation reinforced this interpretation. We previously showed that the remodeling of residual descending pathways mediated this recovery [6,41]. We thus surmised that a small number of nerve fibers had survived the injury, but that these fibers had remained functionally silent due to the hypo-activity below the injury[42].

We previously showed that neurorehabilitation supported by EES mediated a more extensive neurological recovery after incomplete SCI[4], emphasizing the logical importance of residual pathways to promote recovery. Therefore, the development of biological repair interventions remains critical to enhance recovery with neurorehabilitation supported by EES[43,44]. Biomimetic EES may also enable active and sustained movements in the early phase after SCI, allowing to take full advantage of natural repair mechanisms to augment neurological recovery.

The development of the paddle lead required a number of tradeoffs to circumvent the variable topology of the dorsal roots across the human population. While this new lead allowed the validation of our therapeutic concepts, the fixed coverage and uniform distribution of electrodes were inevitably suboptimal. Therefore, we anticipate that delivering this therapy across the human population may require a library of paddle leads or even personalized leads. While current regulations for silicone-based medical devices are not compatible with this possibility, microfabrication processes may provide a realistic path for personalized leads[45,46]. In turn, our computational framework enables selecting the optimal paddle lead for each patient, and planning its surgical positioning for optimal selectivity. With a large choice of leads or increased number of electrodes, the preoperative planning may also be simplified since the the identification of projectomes with fMRI acquisitions would not be necessary. High-density electrode arrays are under development, but the challenge may reside in the availability of pulse generators to control the stimulation. Indeed, biomimetic EES requires neurostimulation platforms designed for closed-loop operations, combining ultrafast and reliable wireless communication with control units that can decode motor intentions from wearable or implanted sensors, including interfaces measuring brain activity [21,47,48].

We only targeted the dorsal roots projecting to the low thoracic segment. However, the selective modulation of trunk muscles suggested that targeting additional thoracic dorsal roots will further improve the recovery of trunk movements[29,49].

These therapeutic concepts are relevant to address other neurological functions that are prioritized by people with SCI[50]. Indeed, EES can regulate bladder and bowel functions[51], hemodynamics[52,53], and arm/hand movements[30]. The regions involved in the regulation of these functions are distributed along the neuraxis, suggesting that purpose-made neurotechnologies targeting the dorsal roots projecting to these specific regions are necessary to develop effective treatments. Targeting some of these functions may require highly-specific stimulation of certain dorsal roots, which could be achieved with the direct neuromodulation of dorsal root ganglia[54].

Scaling up these therapies across clinical centers worldwide will require AI assistants to support neurosurgical interventions and EES program configurations. Advances in machine-learning algorithms and cloud-based computing for medical applications established the technological landscape to realize this transition.

Biomimetic EES restored trunk and leg motor functions within one day after complete sensorimotor paralysis, and mediated the recovery of some independence in ecological settings after neurorehabilitation. This recovery combined with our previous findings in people with incomplete SCI[8] is opening a realistic pathway to deploy a therapy that will mediate clinically meaningful improvements in people presenting with a broad range of SCI severities.

Funding

Supported by Wings for Life, Defitech Foundation, International Foundation for Research in Paraplegia, Rolex for Enterprise, Carigest Promex, Riders4Riders, ALARME, Panacée Foundation, Pictet Group Charitable Foundation, Firmenich Foundation, ONWARD Medical, European Union's Horizon 2020 (No. 785907 Human Brain Project SGA2, No. 842578 and No. 665667), RESTORE: Eurostars E10889, OPTISTIM: Eurostars E!12743, the Swiss National Science Foundation (NCCR Robotics), European Research Council [ERC-2015-CoG HOW2WALKAGAIN 682999], Eurostars No. E10889, the Commission of Technology and Innovation Innosuisse (CTI, No. 41871.1 IP_LS, CTI No. 25761.1), H2020-MSCACOFUND-2015 EPFL Fellows program (No. 665667 to F.B.W.).

Author Contributions Statement

E.B, S.D.H.C and E.P. contributed equally. A.R., S.K., R.D., E.B., F.B., J.R., M.D., C.V., L.M., N.H., M.V., L.B.F., H.L., A.G., Et.P., M.R., K.M., Q.B., L.A., F.B.W., J.B. and G.C. performed experiments and analyzed data. A.R., S.K., R.D., H.M., A.C., B.L., T.N., M.D., N.H., Mi.C., L.B.F., C.H., S.B., S.C., N.G., B.F., N.B., T.D., D.G., J.B., K.M., E.K., N.K., E.N., M.C., F.B.W., J.B. and G.C. designed, developed and/or fabricated hardware and/or software. A.R., S.D.H.C., E.P., H.M., A.C., B.L., T.N., S.B., S.C., N.G., N.K., E.N. and M.C. performed simulations. A.R., E.B., S.D.H.C., E.P., F.B., N.K., J.B.L., E.F., St.M., L.M., R.M., B.N., M.F., A.K., S.M., C.B. and D.V. acquired medical imaging datasets. E.B., A.P., M.T., N.H., M.W., L.G., I.F., V.R., K.K. and G.E. conducted physical therapy. R.D., M.V., A.W., C.J., L.B-F., R.B., V.D., H.L., and L.A. managed regulatory affairs. C.W. handled intellectual property. A.R., S.K., R.D., E.B., S.D.H.C., J.R., L.A. and G.C. prepared illustrations. J.B. performed neurosurgical interventions. G.C. and J.B. conceived and supervised the study. G.C. wrote the paper and all the authors contributed to its editing.

Competing Interests Statement

The authors declare competing financial interests: G.C., J.B., S.M., K.M., F.B.W., M.C. hold various patents in relation with the present work. V.D., D.G., Ju.B., H.L., A.W., C.J., M.C, E.P. are ONWARD employees. G.C. is consultant of ONWARD medical. G.C., J.B., S.M., and V.D. are shareholders of ONWARD, a company with direct relationships with the presented work. N.K. and E.N are shareholders of ZMT Zurich MedTech AG that produces the Sim4Life software. C.W. handles intellectual property for ONWARD medical. The remaining authors declare no competing interests.

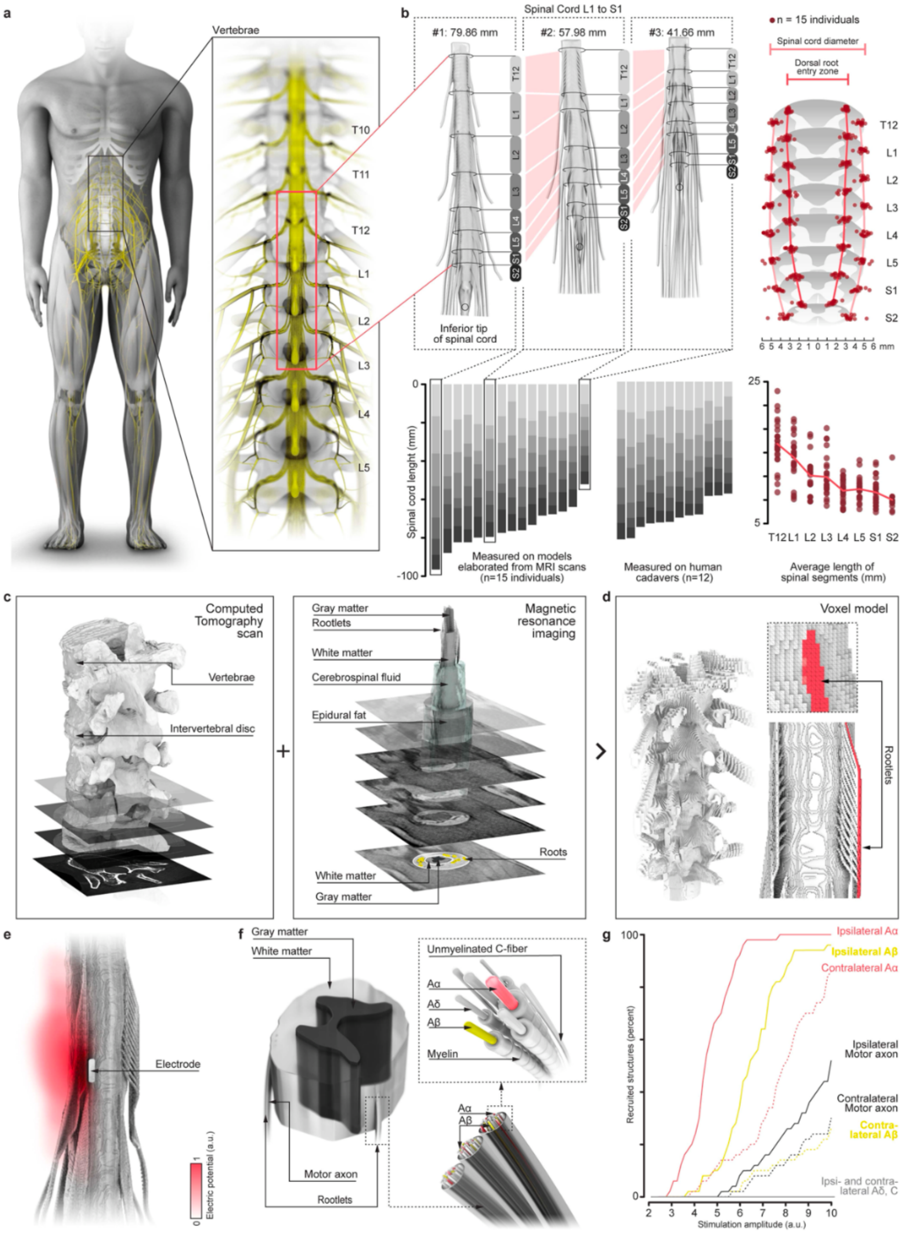

Figure 1: Anatomical quantification and personalizable computational models. a, Human spinal cord, including a visualization of the targeted thoracic, lumbar and sacral dorsal roots. **b,** Spinal cord topology from 27 adult male/female/diverse individuals were quantified from MRI/CT scans of 15 healthy volunteers and anatomical measurements of 12 cadavers. Each bar or dot reports measurements from one individual. Three complete anatomical models are shown from individuals with widely different topologies. **c,** Automated framework to elaborate anatomical models of spinal cord tissues from high-resolution MRI and CT images. **d,** Discretization of anatomical models as voxels using rectilinear (structured) gridding. **e,** Distribution of electric potential when delivering one pulse of EES. **f,** Compartmental cable models incorporating the entire range of afferents and efferents are initialized in the rootlets. **g,** Relative recruitment of afferents and efferents when delivering a single pulse of EES with increasing amplitude.

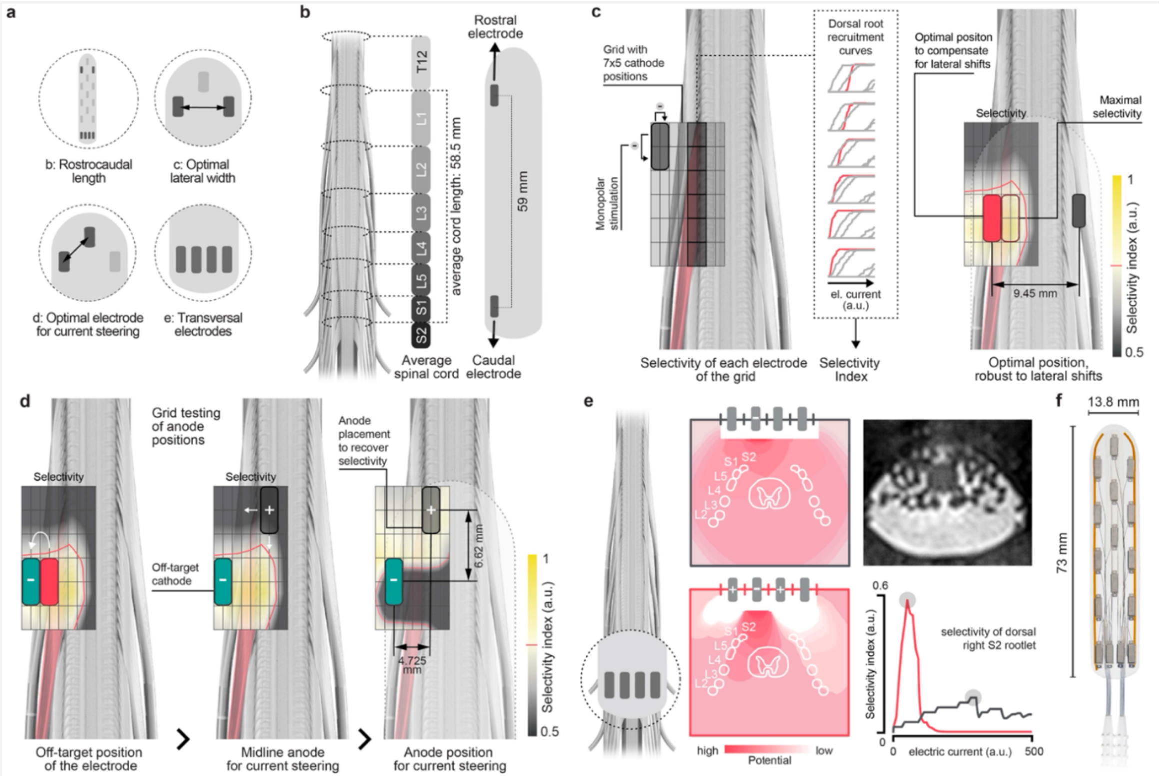

Figure 2: Optimal arrangement of electrodes. **a**, Highlight of the four features that guided the positioning of the electrodes on the new paddle lead. These features were studied using computational experiments detailed in panels b, c, d, and e. **b**, Generalized model reconstructed from averaging all the spinal cords of the atlas. The length of the new paddle lead was calculated from this model. **c**, A grid of 7 x 5 electrodes was positioned over each targeted rootlet bundle, here shown for the L1 dorsal root. Simulations computed a selectivity index for each electrode of the grid to determine the distributions of the lateral electrodes (red rectangle). **d**, Due to the inherent variability of dorsal root distributions and putative deviations during surgical placement, the selectivity of the cathodes may require adjustments (e.g. simulated offset as blue rectangle). Simulations determined that lateral shifts of the cathodes compensate for deviations in the medial direction, while anodes located over the midline steer current with bipolar stimulation. **e**, Distribution of electrical potentials when delivering unipolar versus multipolar stimulation over the dorsal roots agglutinated within the thecal sac. The transverse arrangement of electrodes enables steering the current toward the targeted sacral dorsal roots. **f**, Arrangement of electrodes on the new paddle lead.

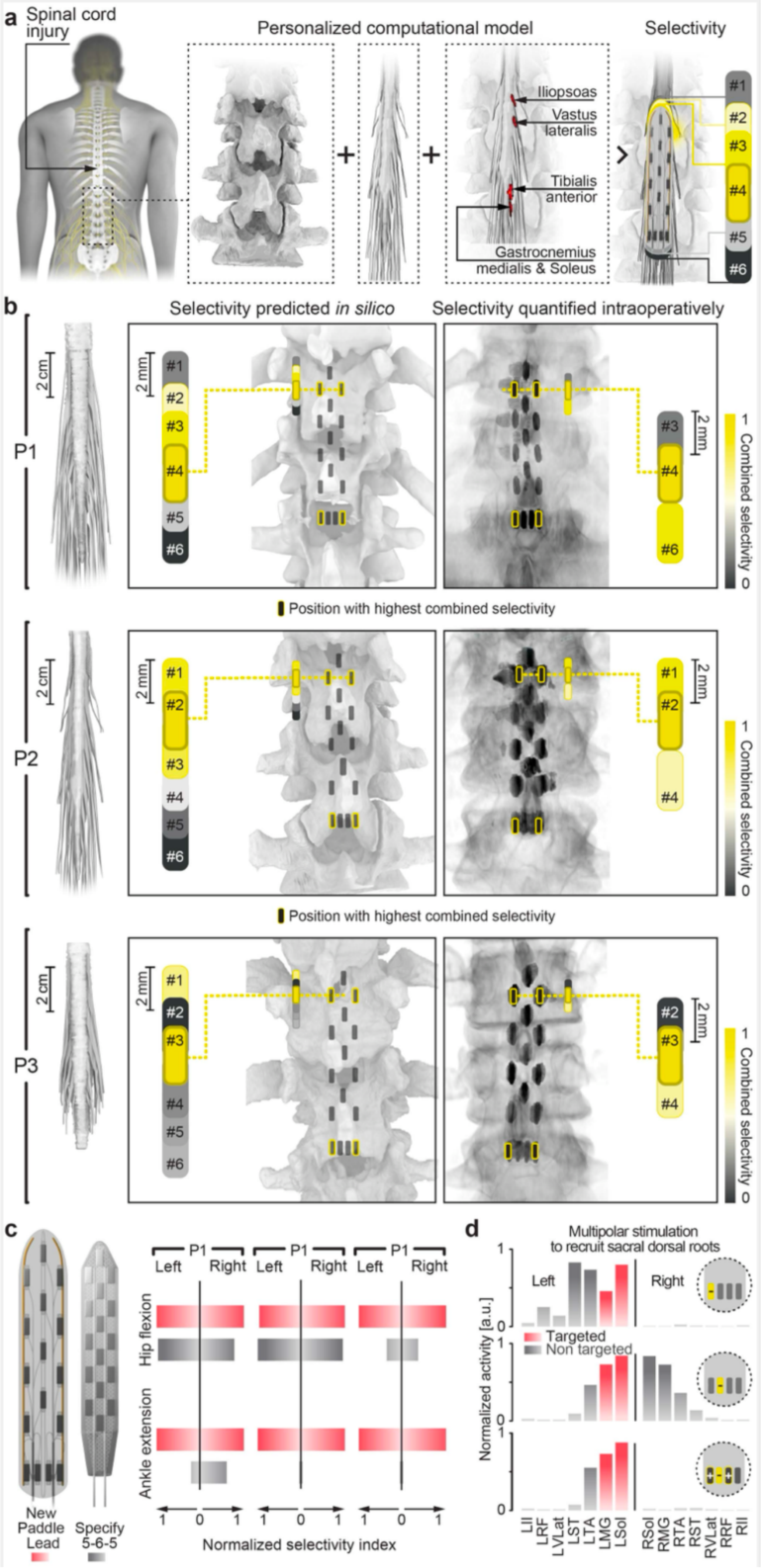
a
Spinal cord injury
Personalized computational model
Iliopsoas
Vastus lateralis
Tibialis anterior
Gastrocnemius medialis & Soleus
Selectivity
#1
#2
#3
#4
#5
#6
b
Selectivity predicted *in silico*
Selectivity quantified intraoperatively
P1
2 cm
2 mm
Combined selectivity
1
0
Position with highest combined selectivity
P2
P3
c
P1
Left
Right
Hip flexion
Ankle extension
Normalized selectivity index
1
0
1
New Paddle Lead
Specify 5-6-5
d
Multipolar stimulation to recruit sacral dorsal roots
Normalized activity [a.u.]
Left
Right
Targeted
Non targeted
LII
LRF
LVLat
LST
LTA
LMG
LSol
RSol
RMG
RTA
RST
RVLat
RRF
RII

Figure 3: Preoperative planning and intraoperative validation. a, CT scan combined with structural and functional MRI acquisitions enabled the personalization of computational models predicting the interactions between the location of EES and the recruitment of afferents in the dorsal roots. **b,** for each participant, simulations (left) calculated the relative selectivity of the paddle lead for 6 positions separated by 2 mm, as shown in the vertical bars positioned over the computational model, and their enlarged version next to each bar. The selectivity of electrodes located at each corner of the paddle lead is aggregated in a combined (color coded) selectivity index. The same procedure was conducted intraoperatively (right) for three positions of the paddle lead, including the optimal position predicted by the model. Representations are the same as in the computational simulations. The final surgical positioning of the paddle lead is displayed in the reconstructed CT images. **c,** Bar plots reporting the selectivity of electrodes from the new paddle lead (in red) and Specify 5-6-5 (in grey) to recruit muscles eliciting hip flexion and ankle extension. **d,** Bar plots reporting the amplitude of muscle responses when stimulating with monopolar versus multipolar electrode configurations, showing the ability of the transverse electrode arrangement to selectively recruit sacral roots despite the agglutination of all lumbar dorsal roots within the stimulated region.

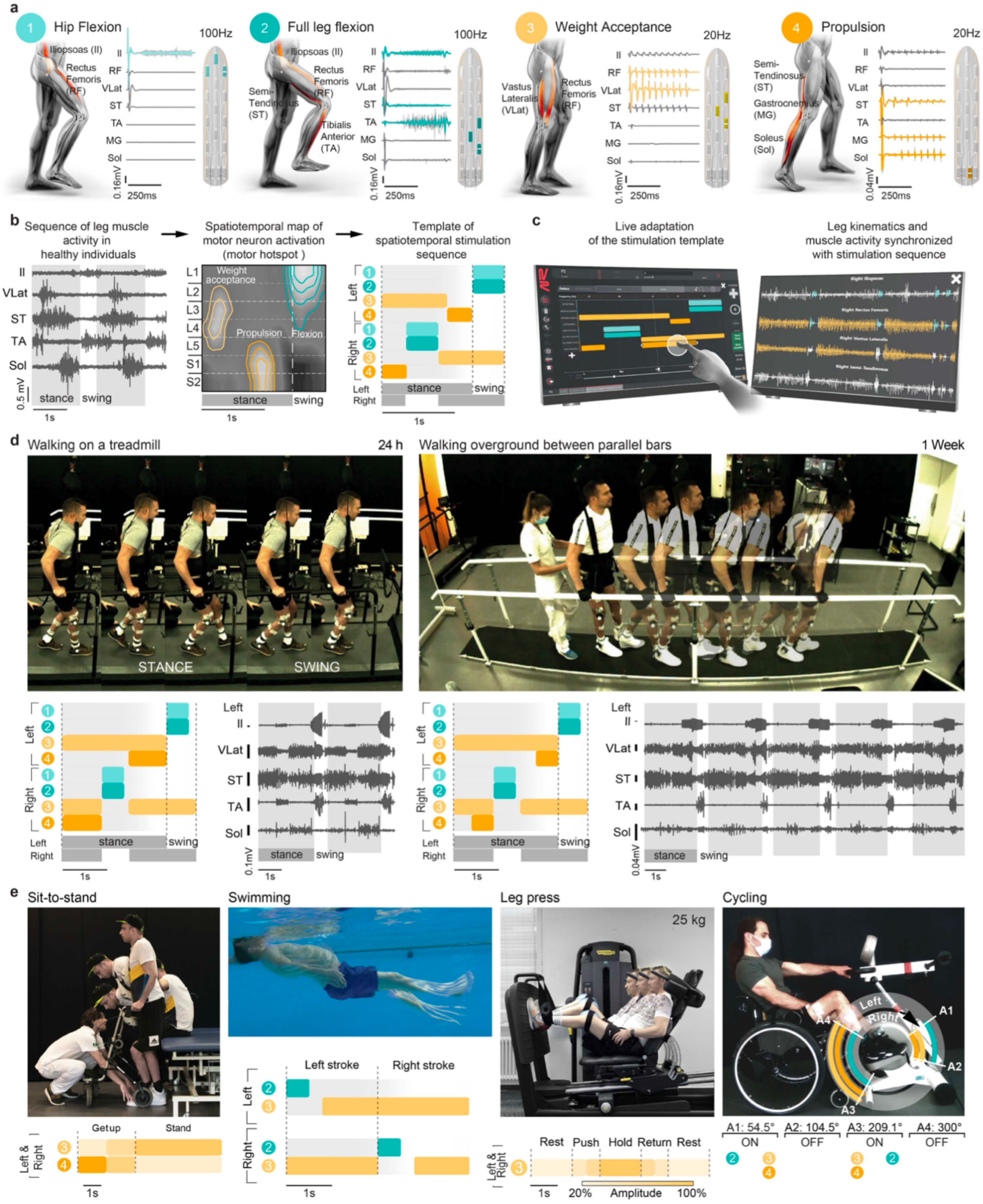

Figure 4: Configuration of activity-dependent stimulation programs. a, Library of optimized anode and cathode configurations and stimulation frequencies to modulate motor pools associated with the key phases of gait, as highlighted with the color code. **b,** Sequence of muscle activity underlying walking in healthy people, converted into a spatiotemporal map of motor neuron activity that highlights the timing and location of motor hotspot activation; translated into a preprogrammed sequence of stimulation bursts (template) that aims to reproduce this activation pattern. Color code as in (a). The configurations of electrodes targeting each hotspot are derived from the library, and injected into this template. **c,** Software enabling live adjustments of stimulation patterns and parameters based on real-time feedback

from muscle activity and kinematic sensors that are synchronized with stimulation sequences. **d,** Walking on a treadmill with stimulation after less than one hour of configuration, including sequence of stimulation and underlying muscle activity. **e,** Independent walking between parallel bars less than one week after the onset of the therapy. **f,** Chronophotography of sit-to-stand, swimming, leg-press and motomed exercises enabled by activity-specific stimulation programs, displayed at the bottom of each chronophotography.

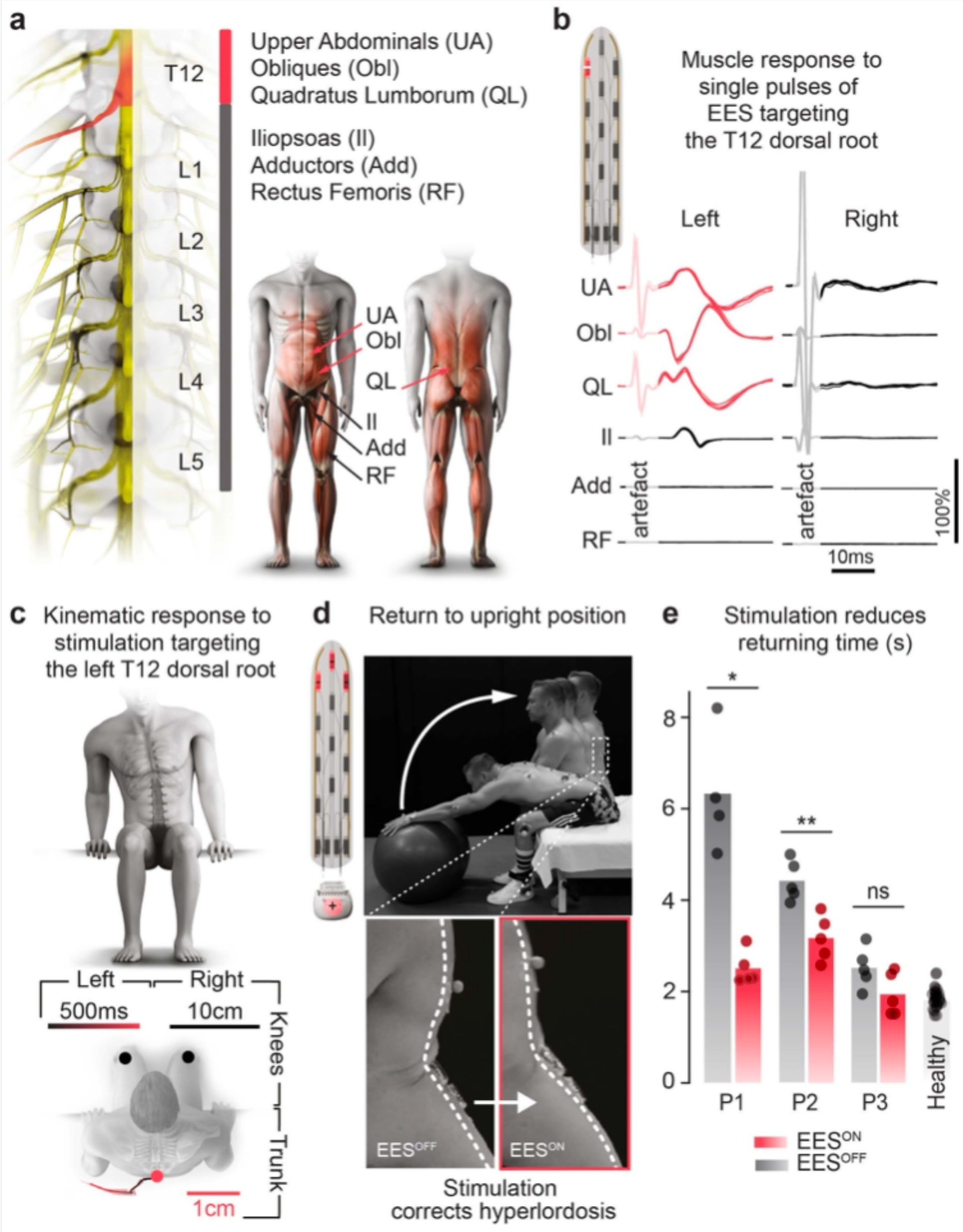

Figure 5: Configuration of trunk-specific stimulation programs. a, Stimulation of the dorsal root projections to the T12 spinal segment modulates trunk and abdominal muscles, **b,** as shown in muscle responses. **c,** Temporal course (color-coded) of coronal plane trunk trajectory elicited by side-specific stimulation. **d,** Chronophotography of a sequence of trunk flexion and extension. The onsets highlight trunk posture at rest without and with a stimulation program optimized for modulation of motor pools innervating trunk muscles. **e,** bar plots reporting the time necessary to complete the return phase (extension) of the flexion / extension sequence of trunk movements for the 3 participants, compared to 5 healthy individuals (Mann-Whitney test, two-tailed, P1: p= 0.0159, P2: p= 0.0079, P3: p= 1429, *, p<0.05; **, p<0.01). Dots represent the number of repeated movements for each patient (N=5 repetitions per patient and per stimulation condition)

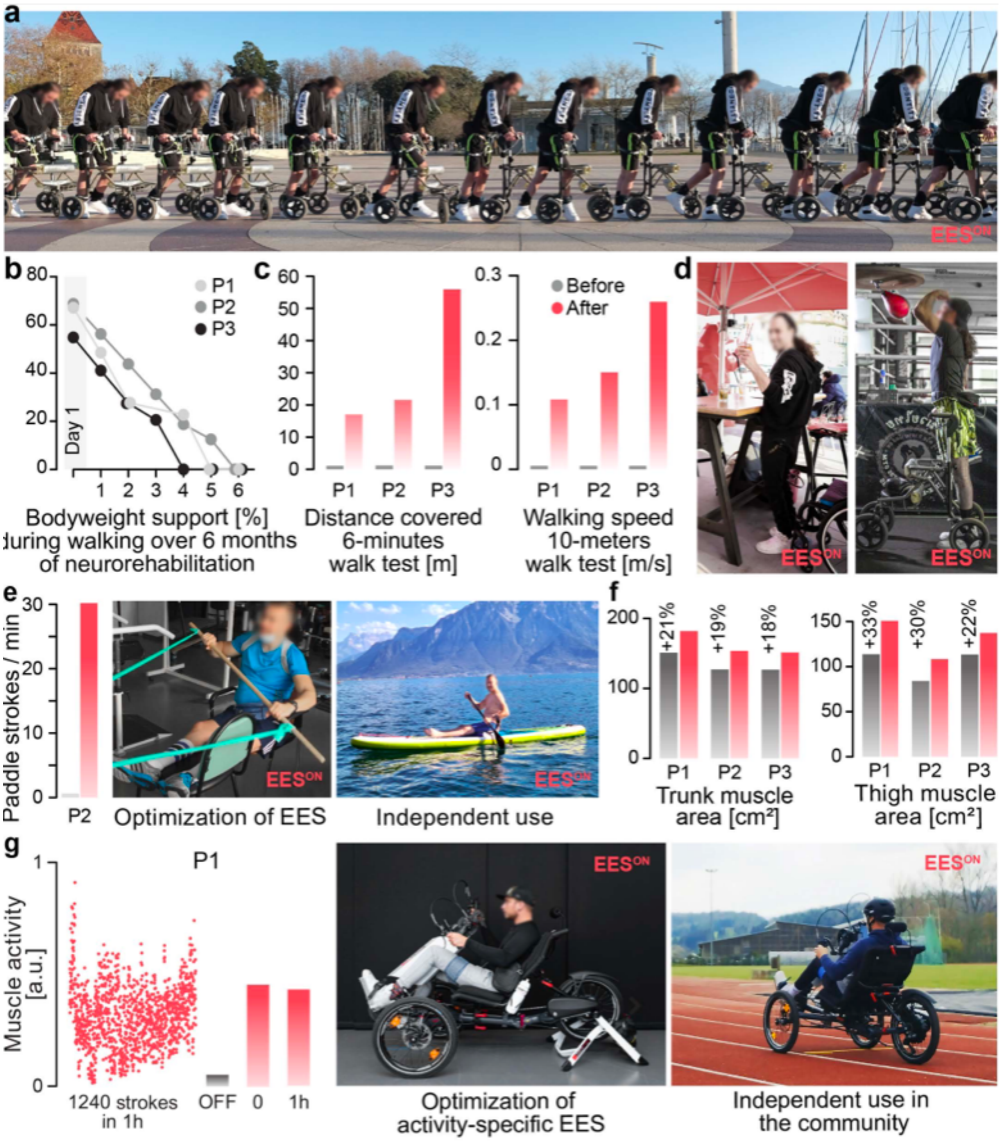

Figure 6: Recovery of independence in the community. **a**, Chronophotography of independent walking outdoors after 6 months of practice with activity-specific programs. **b,** Optimal bodyweight support to enable walking during neurorehabilitation. **c,** Bar plots reporting performance in the six-minute walk test and ten-meter walk test before and after neurorehabilitation with activity-specific stimulation programs. No assistance was provided during these tests. **d,** Standing for extensive periods of time for boxing or enjoying a drink at a high table of a bar. See also **Supplementary Video 4. e,** Stimulation programs for trunk stability while paddling were developed in the lab, and then used to support paddling activity on a lake. Bar plots report the number of paddle strokes per minute with and without EES. **f,** Bar plots reporting changes in thigh and trunk muscle mass, quantified as total/specific cross-sectional area. **g,** Amplitude of muscle activity for each of N=1240 strokes performed over one hour. Bar plots report the mean amplitude of muscle activity without EES (N=27 cycles, gray), and calculated during the N=100 first and N=100 last cycles (red). Photographs illustrate the setting for the development of cycling stimulation, and its use community settings.

References

1. Ichiyama, R. M. *et al.* Step training reinforces specific spinal locomotor circuitry in adult spinal rats. *The Journal of neuroscience : the official journal of the Society for Neuroscience* **28**, 7370–7375 (2008).

2. Courtine, G. et al. Transformation of nonfunctional spinal circuits into functional states after the loss of brain input. *Nat Neurosci* **12**, 1333–1342 (2009).

3. Wenger, N. et al. Closed-loop neuromodulation of spinal sensorimotor circuits controls refined locomotion after complete spinal cord injury. *Sci Transl Med* **6**, 255ra133-255ra133 (2014).

4. Wenger, N. et al. Spatiotemporal neuromodulation therapies engaging muscle synergies improve motor control after spinal cord injury. *Nat Med* **22**, 138–145 (2016).

5. Brand, R. van den et al. Restoring Voluntary Control of Locomotion after Paralyzing Spinal Cord Injury. *Science* **336**, 1182–1185 (2012).

6. Asboth, L. et al. Cortico–reticulo–spinal circuit reorganization enables functional recovery after severe spinal cord contusion. Nat Neurosci **21**, 576–588 (2018).

7. Gill, M. L. et al. Neuromodulation of lumbosacral spinal networks enables independent stepping after complete paraplegia. *Nature medicine* **24**, 1677–1682 (2018).

8. Wagner, F. B. et al. Targeted neurotechnology restores walking in humans with spinal cord injury. Nature **563**, 65–71 (2018).

9. Harkema, S. et al. Effect of epidural stimulation of the lumbosacral spinal cord on voluntary movement, standing, and assisted stepping after motor complete paraplegia: a case study. *Lancet* **377**, 1938–1947 (2011).

10. Angeli, C. A. et al. Recovery of Over-Ground Walking after Chronic Motor Complete Spinal Cord Injury. *New Engl J Med* **379**, 1244–1**25**0 (2018).

11. Danner, S. M. et al. Human spinal locomotor control is based on flexibly organized burst generators. *Brain : a journal of neurology* **138**, 577–588 (2015).

12. Formento, E. et al. Electrical spinal cord stimulation must preserve proprioception to enable locomotion in humans with spinal cord injury. Nat Neurosci 21, 1728–1741 (2018).

13. Herman, R., He, J., D'Luzansky, S., Willis, W. & Dilli, S. Spinal cord stimulation facilitates functional walking in a chronic, incomplete spinal cord injured. *Spinal cord : the official journal of the International Medical Society of Paraplegia* **40**, 65–68 (2002).

14. Barolat, G., Myklebust, J. B. & Wenninger, W. Enhancement of Voluntary Motor Function Following Spinal Cord Stimulation - Case Study. *Stereot Funct Neuros* **49**, 307–314 (1986).

15. DIMITRIJEVIC, M. R., GERASIMENKO, Y. & PINTER, M. M. Evidence for a Spinal Central Pattern Generator in Humansa. *Ann Ny Acad Sci* **860**, 360–376 (1998).

16. Darrow, D. et al. Epidural Spinal Cord Stimulation facilitates immediate restoration of dormant motor and autonomic supraspinal pathways after chronic neurologically complete spinal cord injury. *Journal of neurotrauma* (2019).

17. Gerasimenko, Y. P. et al. Spinal cord reflexes induced by epidural spinal cord stimulation in normal awake rats. *Journal of neuroscience methods* **157**, 253–263 (2006).

18. Rattay, F. et al. Mechanisms of electrical stimulation with neural prostheses. *Neuromodulation : journal of the International Neuromodulation Society* **6**, 42–56 (2003).

19. Capogrosso, M. et al. A Computational Model for Epidural Electrical Stimulation of Spinal Sensorimotor Circuits. *J Neurosci* **33**, 19326–19340 (2013).

20. Moraud, E. M. et al. Mechanisms Underlying the Neuromodulation of Spinal Circuits for Correcting Gait and Balance Deficits after Spinal Cord Injury. *Neuron* **89**, 814–828 (2016).

21. Capogrosso, M. et al. A brain–spine interface alleviating gait deficits after spinal cord injury in primates. Nature **539**, 284–288 (2016).
22. Minev, I. R. et al. Electronic dura mater for long-term multimodal neural interfaces. Science **347**, 159–163 (2015).
23. Capogrosso, M. et al. Configuration of electrical spinal cord stimulation through real-time processing of gait kinematics. *Nat Protoc* **13**, 2031–2061 (2018).
24. Yakovenko, S., Mushahwar, V., VanderHorst, V., Holstege, G. & Prochazka, A. Spatiotemporal Activation of Lumbosacral Motoneurons in the Locomotor Step Cycle. *J Neurophysiol* **87**, 1542–1553 (2002).
25. Cappellini, G., Ivanenko, Y. P., Dominici, N., Poppele, R. E. & Lacquaniti, F. Migration of motor pool activity in the spinal cord reflects body mechanics in human locomotion. *Journal of neurophysiology* **104**, 3064–3073 (2010).
26. Molnar, G. & Barolat, G. Principles of Cord Activation During Spinal Cord Stimulation. *Neuromodulation Technology Neural Interface* **17**, 12–21 (2014).
27. Minassian, K., Hofstoetter, U., Tansey, K. & Mayr, W. Neuromodulation of lower limb motor control in restorative neurology. *Clinical neurology and neurosurgery* **114**, 489–4**97** (2012).
28. Moraud, E. M. et al. Closed-loop control of trunk posture improves locomotion through the regulation of leg proprioceptive feedback after spinal cord injury. *Scientific reports* **8**, 76 (2018).
29. Gill, M. et al. Epidural Electrical Stimulation of the Lumbosacral Spinal Cord Improves Trunk Stability During Seated Reaching in Two Humans With Severe Thoracic Spinal Cord Injury. *Frontiers Syst Neurosci* **14**, 79 (2020).
30. Greiner, N. et al. Recruitment of upper-limb motoneurons with epidural electrical stimulation of the cervical spinal cord. *Nat Commun* **12**, 435 (2021).
31. Neufeld, E., Szczerba, D., Chavannes, N. & Kuster, N. A novel medical image data-based multi-physics simulation platform for computational life sciences. *Interface Focus* **3**, 20120058 (2013).
32. Kinany, N., Pirondini, E., Micera, S. & Ville, D. V. D. Dynamic Functional Connectivity of Resting-State Spinal Cord fMRI Reveals Fine-Grained Intrinsic Architecture. Neuron **108**, 4**24-**435.e4 (2020).
33. Landelle, C. et al. Functional brain changes in the elderly for the perception of hand movements: A greater impairment occurs in proprioception than touch. *Neuroimage* **220**, 117056 (2020).
34. Courtine, G., Nunzio, A. M. D., Schmid, M., Beretta, M. V. & Schieppati, M. Stance- and Locomotion-Dependent Processing of Vibration-Induced Proprioceptive Inflow From Multiple Muscles in Humans. Journal of neurophysiology **9**7, 772–779 (2007).
35. Roll, J. P., Vedel, J. P. & Ribot, E. Alteration of proprioceptive messages induced by tendon vibration in man: a microneurographic study. *Exp Brain Res* **76**, 213–222 (1989).
36. Pierrot-Deseilligny, E. & Burke, D. The Circuitry of the Human Spinal Cord. (2005) doi:10.1017/cbo9780511545047.
37. Lempka, S. F. et al. Patient-Specific Analysis of Neural Activation During Spinal Cord Stimulation for Pain. Neuromodulation Technology Neural Interface **23**, 572–581 (2020).
38. Capogrosso, M. et al. Configuration of electrical spinal cord stimulation through real-time processing of gait kinematics. *Nature Protocols* (2018).
39. Mignardot, J.-B. et al. A multidirectional gravity-assist algorithm that enhances locomotor control in patients with stroke or spinal cord injury. Sci Transl Med 9, eaah3621 (2017).
40. Shokur, S., Mazzoni, A., Schiavone, G., Weber, D. J. & Micera, S. A modular strategy for

next-generation upper-limb sensory-motor neuroprostheses. Med (2021) doi:10.1016/j.medj.2021.05.002.

41. Brand, R. van den et al. Restoring Voluntary Control of Locomotion after Paralyzing Spinal Cord Injury. Science 336, 1182–1185 (2012).

42. Edgerton, V. R. & Harkema, S. Epidural stimulation of the spinal cord in spinal cord injury: current status and future challenges. *Expert Review of Neurotherapeutics* **11**, 1351–1353 (2011).

43. Courtine, G. & Sofroniew, M. V. Spinal cord repair: advances in biology and technology. Nature medicine 25, 898–908 (2019).

44. Morse, L. R. et al. Meeting Proceedings for SCI 2020: Launching a Decade of Disruption in Spinal Cord Injury Research. *J Neurotraum* **38**, 1251–1266 (2021).

45. Schiavone, G. et al. Soft, Implantable Bioelectronic Interfaces for Translational Research. *Adv Mater* **32**, 1906512 (2020).

46. Barra, B. et al. Epidural Electrical Stimulation of the Cervical Dorsal Roots Restores Voluntary Arm Control In Paralyzed Monkeys. *Biorxiv* 2020.11.13.379750 (2021) doi:10.1101/2020.11.13.379750.

47. Bonizzato, M. et al. Brain-controlled modulation of spinal circuits improves recovery from spinal cord injury. Nat Commun 9, (2018).

48. MD, P. A. L. B. et al. An exoskeleton controlled by an epidural wireless brain–machine interface in a tetraplegic patient: a proof-of-concept demonstration. *The Lancet Neurology* 1–11 (2019) doi:10.1016/s1474-4422(19)30321-7.

49. Chen, C.-L. et al. The relationship between sitting stability and functional performance in patients with paraplegia1 1No commercial party having a direct financial interest in the results of the research supporting this article has or will confer a benefit upon the author(s) or upon any organization with which the author(s) is/are associated. *Arch Phys Med Rehab* **84**, 1276–1281 (2003).

50. Anderson, K. D. Targeting recovery: priorities of the spinal cord-injured population. Journal of neurotrauma 21, 1371–1383 (2004).

51. Herrity, A. N., Williams, C. S., Angeli, C. A., Harkema, S. J. & Hubscher, C. H. Lumbosacral spinal cord epidural stimulation improves voiding function after human spinal cord injury. Scientific reports 8, 8688 (2018).

52. Squair, J. W. et al. Neuroprosthetic baroreflex controls haemodynamics after spinal cord injury. Nature **590**, 308–314 (2021).

53. Ditterline, B. E. L. et al. Beneficial Cardiac Structural and Functional Adaptations After Lumbosacral Spinal Cord Epidural Stimulation and Task-Specific Interventions: A Pilot Study. *Front Neurosci-switz* **14**, 554018 (2020).

54. Soloukey, S. et al. The Dorsal Root Ganglion as a Novel Neuromodulatory Target to Evoke Strong and Reproducible Motor Responses in Chronic Motor Complete Spinal Cord Injury: A Case Series of Five Patients. Neuromodulation Technology Neural Interface 24, 779–793 (2021).

55. Schirmer, C. M. et al. Heuristic map of myotomal innervation in humans using direct intraoperative nerve root stimulation: Clinical article. *J Neurosurg Spine* **15**, 64–70 (2011).

Extended data figures

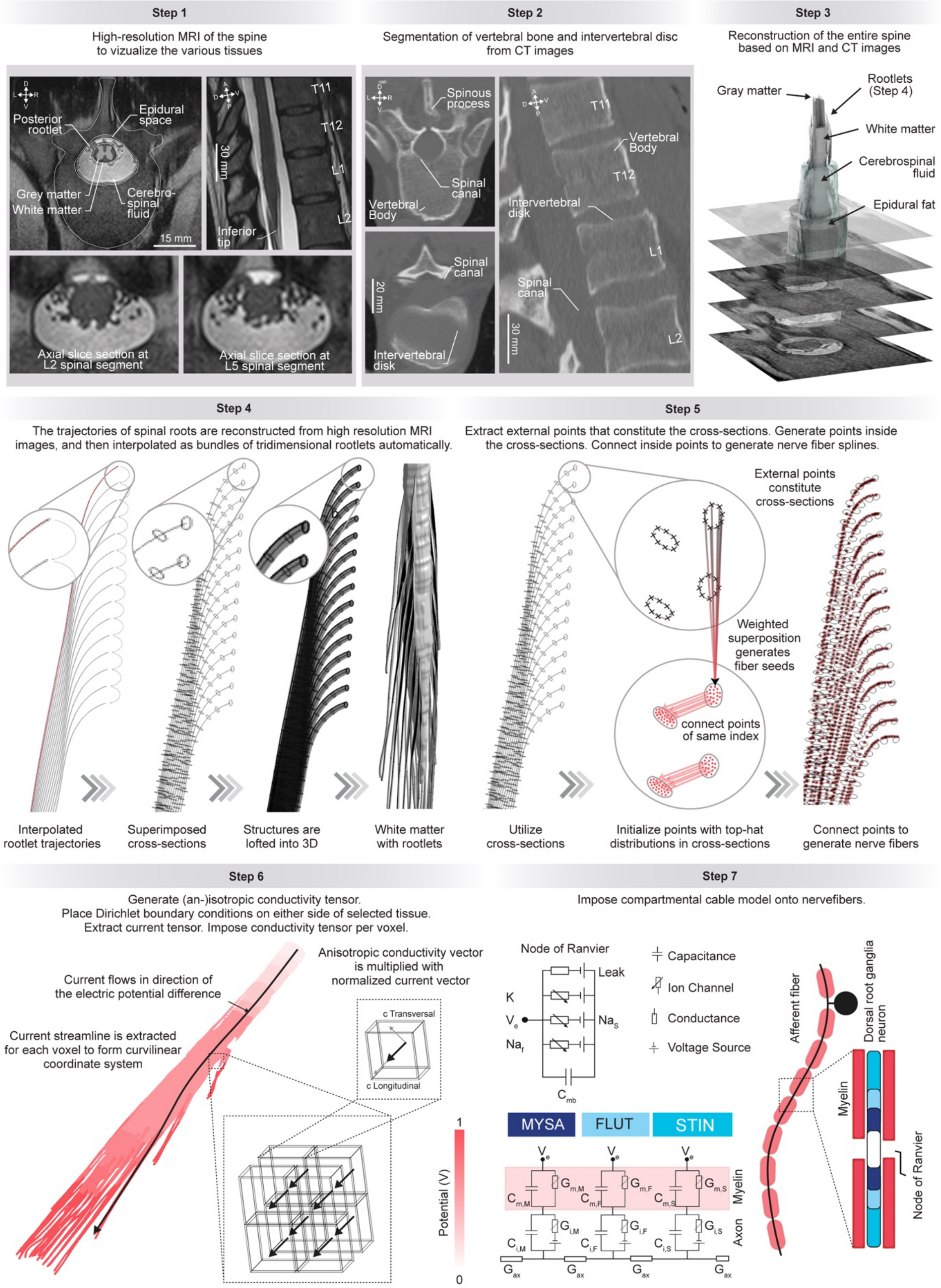

Extended Data Figure 1: Personalizable computational models of the interactions between EES and the spinal cord. Step 1, High-resolution MRI images enable clear-cut visualization of spinal tissues, including individual dorsal roots. **Step 2,** CT images enable reconstructing the tridimensional geometry of vertebral bodies. **Step 3,** Elaboration of highly realistic anatomical models from MRI and CT scans. **Step 4,** Automatic generation of rootlets based on the identification of the uppermost rootlet (shown in red) in high-resolution MRI acquisitions. Rootlet trajectories are interpolated from this rootlet, using the measured segment length as a reference. **Step 5**, Splines representing the nerve fibers are automatically generated inside the rootlets. For this purpose, points are initialized in each cross-section based on a weighted superposition of the points constituting the cross-section itself. These points are connected to generate splines. **Step 6,** Conductivity maps are imposed on each voxel of the discretized finite element models. The white matter and rootlets require an anisotropic conductivity map. Functionality has been implemented in Sim4Life for that purpose that generates anisotropic conductivity maps by solving a diffusion problem with suitable boundary conditions in the tissues of interest and locally aligning conductivity tensors with the gradient of the obtained solution. **Step 7,** Compartmental cable models are initialized along each spline to integrate the nerve fibers.

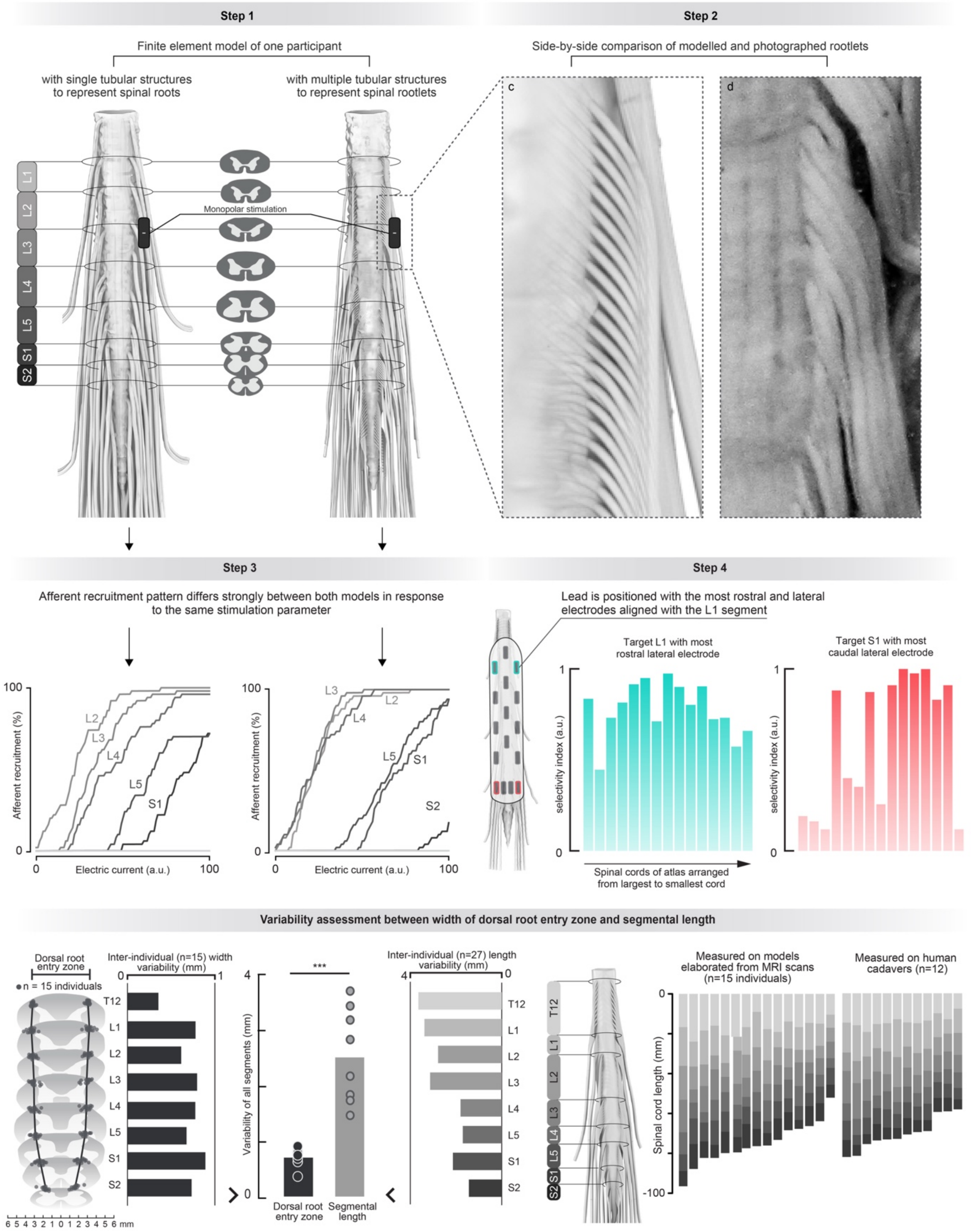

Extended Data Figure 2: Importance of modeling rootlet bundles. Step 1, Models of the same spinal cord wherein the dorsal roots are modelled as single tubular structures (left) versus multiple tubular structures mimicking the topology of rootlet bundles observed in humans (right), as shown in **Step 2,** side by side comparison of the rootlet bundles in the model and in a real spinal cord. To create the model of the rootlets, we determined the entry point of the uppermost rootlet for each spinal segment, and then populated the space from the uppermost rootlet of a given dorsal root to the uppermost rootlet of the next dorsal root by distributing rootlets homogeneously across this space. **Step 3,** A pulse of EES was delivered with increasing intensities through the electrode depicted in step 1, over the L3 dorsal root. The plots show the resulting recruitment curve of each dorsal root. The explicit models of rootlets led to pronounced differences in the recruitment curves of each dorsal root. **Step 4,** Performance of the new paddle lead evaluated in 15 computational models of the atlas. The top left electrode of the paddle lead was positioned over the dorsal root innervating the L1 spinal segment, as depicted in the model on the left. The plot on the left reports the selectivity of this electrode for each model, organized laterally based on the length of the spinal cord (as reported in Fig. 1). The plot on the right reports the selectively of the bottom left electrode to recruit the dorsal root projecting to the S1 spinal segment. **Lower Panel,** Horizontal bar plots on the left report the variability of the width of the dorsal root entry zone (n = 15 healthy volunteers). Horizontal bar plots on the right report the variability of length of each spinal segment (n = 27 spinal cords). The bar plot between these two plots reports the variability of the width of the dorsal root entry zones and of the length of spinal segments. $p = 0.000035$, ***, $P < 0.0001$, two-tailed t-test.

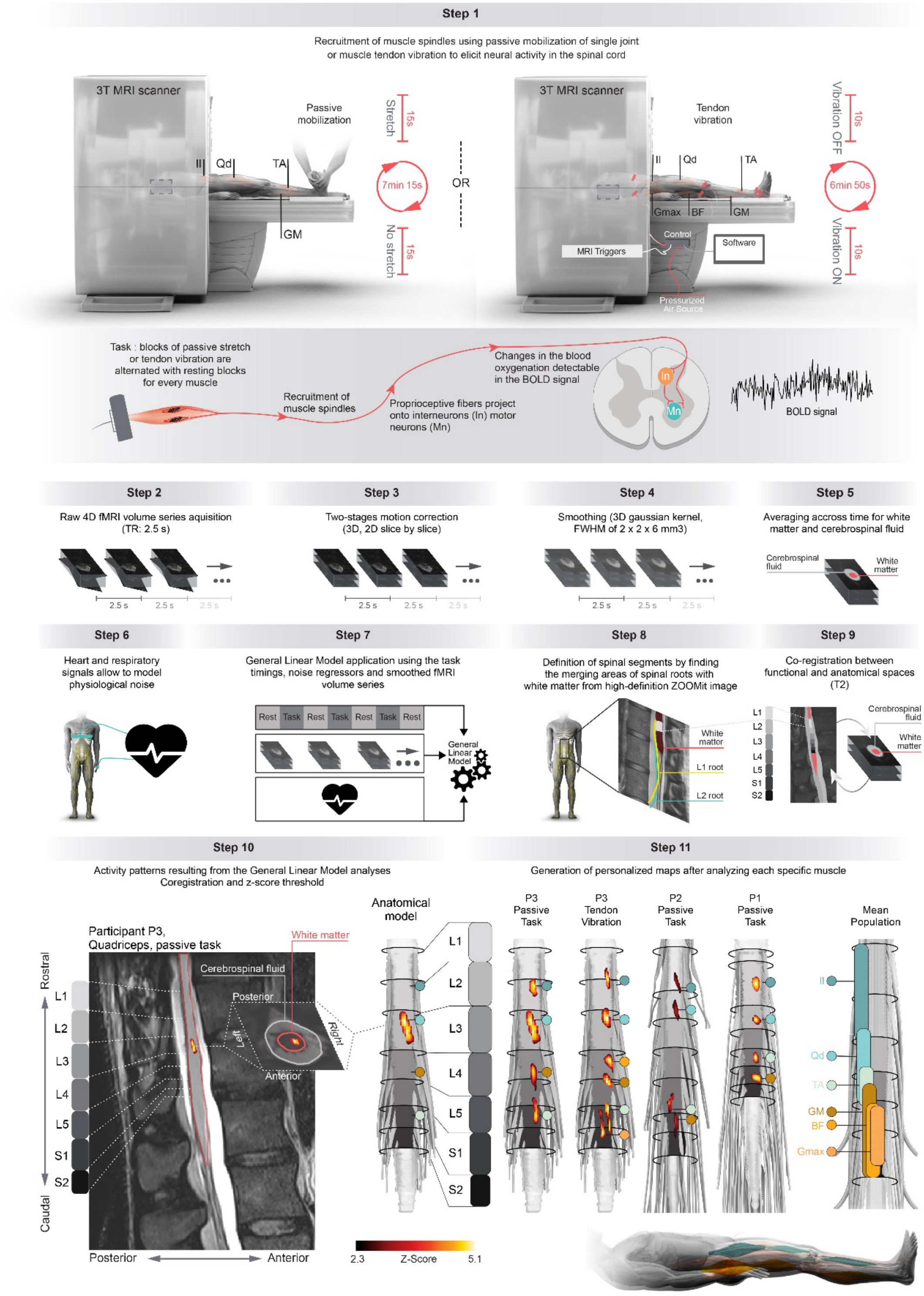

Extended Data Figure 3: Identification of the projectome from propriospinal neurons. Step 1, Acquisition of functional MRI from the spinal cord in response to the recruitment of proprioceptive afferents from specific leg muscles. The muscle spindles are recruited either by stretching the muscles in which they are embedded (the limb is mobilized by a physiotherapist, aided with audio cues), or by applying muscle tendon vibration using MR-compatible pneumatic vibrators (synchronized with MRI triggers). Two runs are acquired for each muscle. Only the right leg muscles are tested. In addition to the functional volume series, T2 anatomical images and physiological (heart rate, respiratory) signals are acquired. **Step 2**, Raw fMRI volume series are repeatedly acquired every 2.5 s (TR) in functional runs lasting about 7 minutes. **Step 3,** A two staged motion correction (3D and then 2D slice-by-slice) is applied for each run. First, the volumes are registered to their respective averaged-in-time image using 3D rigid body realignment. Secondly, taking as reference the averaged-in-time corrected volume, a slice-by-slice 2D realignment is applied thus accounting for the non rigid property of the spinal cord. **Step 4,** The motion corrected series are spatially smoothed, volume by volume with 3D gaussian kernel with full width at half maximum (FWHM) of $2x2x6mm^3$. **Step 5,** The motion-corrected series are again averaged through time. The cerebrospinal fluid and white matter are segmented from this mean functional image. **Step 6**, Physiological signals (heart rate and respiratory) acquired concomitantly to the fMRI volumes are used to model physiological noise (RETROICOR based procedure). If no signals are available, noise regressors are built with component based noise extraction (aCompCor). **Step 7**, Acquisition timings corresponding to the task-design, pre-processed (motion corrected, smoothed) fMRI volume series and physiological noise regressors are submitted to a specific first level generalized linear model. A second level fixed effects analysis (subject level, task specific) is performed by combining the two runs. Whenever possible, multiple comparison corrections are performed ($Z > 2$, $p_{corr} < 0.05$). **Step 8**, Spinal segments are identified from high-definition T2-ZOOMit structural images that allow visualization of the dorsal roots. Spinal segments are then reported in the T2 anatomical image acquired in each run. **Step 9**, Using non-rigid transformations, the mean functional images are co-registered to the T2 anatomical image. **Step 10**, Thresholded activity patterns resulting from the generalized linear model are coregistered to the anatomical image. The projectome of proprioceptive neurons innervating the mobilized muscles are extracted and mapped to the anatomical model. **Step 11**, Projectomes from the three participants, and for comparison, averaged myotome distribution measured electrophysiologically in a large population of patients undergoing surgery. The color dots represent reconstructed projectome from key leg muscles. Vertical color bars represent mean population distribution of muscular motor hotpots. The projectomes differed across the participants. In particular, the projectome identified in P3 revealed an unexpected inversion of the projectome from ankle antagonists. This rostrocaudal inversion was confirmed electrophysiologically.

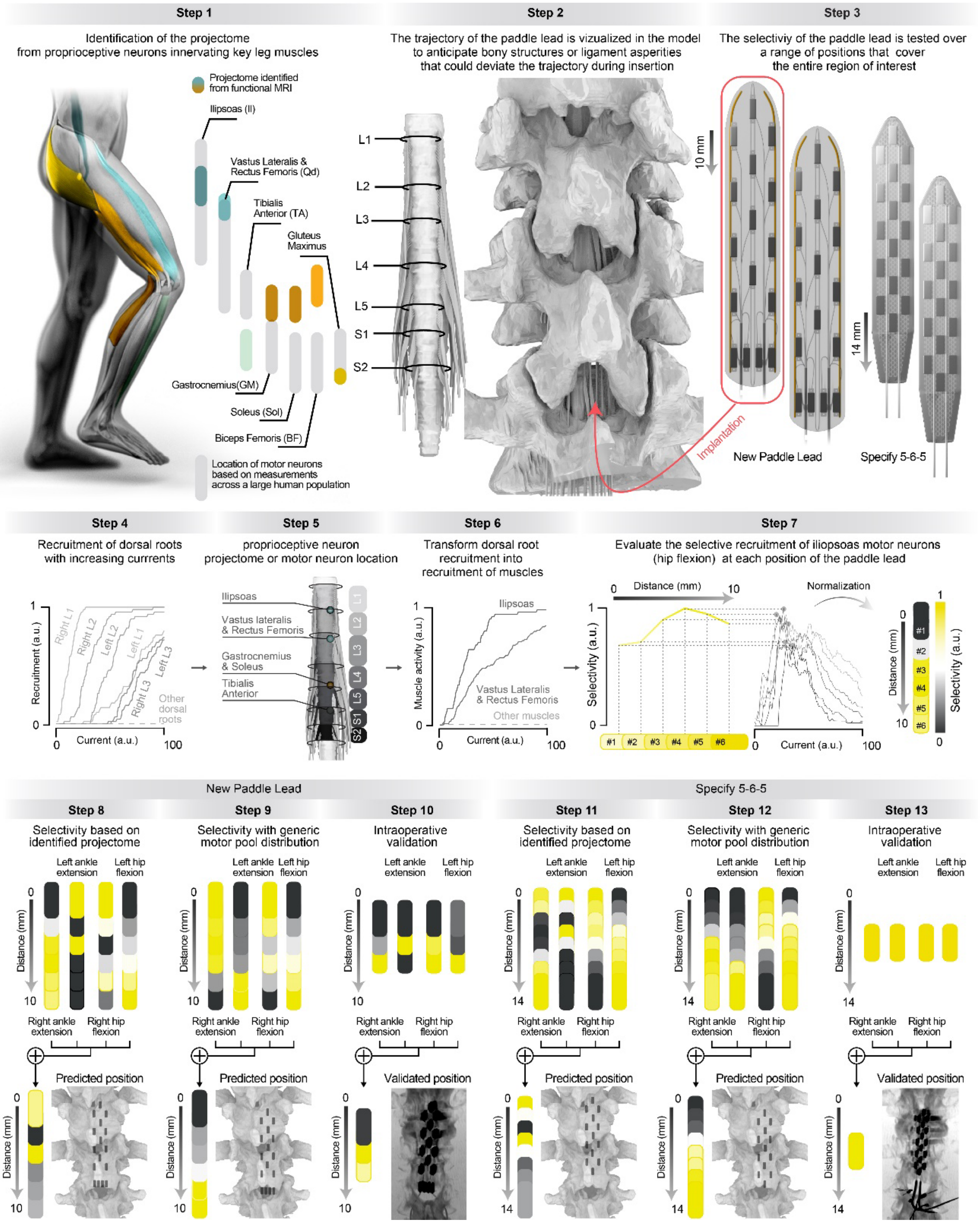

Extended Data Figure 4: Preoperative planning for optimal placement of the new paddle lead. Step 1, CT, structural MRI and functional MRI acquisitions allow to personalize a computational model of the interactions between EES and the spinal cord for each participant. **Step 2,** The insertion of the new paddle lead within the spinal canal is visualized in the model to anticipate bony structures or ligaments that could deviate the trajectory. **Step 3,** The new paddle lead is positioned at 6 locations separated by 2 mm, thus covering the entire region of the spinal cord targeted by the therapy. The same procedure was applied to the Specify 5-6-5 lead, except that 2 additional locations were necessary to cover the entire region since this lead is shorter than the new paddle lead. **Step 4,** The plot shows the recruitment of each dorsal root when simulating the delivery of EES at increasing intensities through the top left electrode of the paddle lead. The same simulations were performed for the electrodes located at each corner of the paddle lead. **Step 5,** The recruitment of dorsal roots is translated into the recruitment of motor pools based on a transformation matrix that maps the recruitment of afferents to the recruitment of motor pools. The transformation matrix was either based on the averaged location of motor pools across the human population[55], or the projectome of proprioceptive neurons from key leg muscles identified from functional MRI. **Step 6,** Applying the transformation matrix depicted in Step 5 allows to convert the predicted recruitment of dorsal roots shown in Step 4 into a prediction of motor pool recruitment. **Step 7,** For each position of the lead, the recruitment of the targeted motor pools compared to the non-targeted motor pools is measured to obtain a selectivity index. For example, the recruitment of the dorsal root projecting to the L1 spinal segments intends to recruit the motor neurons innervating the iliopsoas muscle to elicit hip flexion. The relative recruitment of the iliopsoas muscle versus the rectus femoris or vastus lateralis muscles is transformed into a selectivity index. For each position of the paddle lead, the selectivity index for the tested electrode is color coded, and the selectivity between the tested locations interpolated to obtain a continuum. **Step 8,** The selectivity indices obtained for the electrodes located at each corner of the paddle lead (from left to right, targeting motor neurons eliciting hip flexion or ankle extension) are aggregated into a combined selectivity index that defines the performance of the paddle lead at the tested position. The optimal position for the paddle lead was defined as the position for which the highest combined selectivity index was obtained (most yellow rectangle). **Step 9,** Optimal position of the new paddle lead predicted based on a personalized computational model but a generic distribution of motor neuron locations. **Step 10,** Intraoperative quantification of the combined selectivity index, and thus identification of the optimal position of the new paddle lead. The predicted optimal position of the paddle lead based on a personalized model with the identified projectomes of proprioceptive neurons matched the optimal position validated intraoperatively, whereas simulations based on the averaged location of motor pools across the human population failed to predict the optimal position. **Step 11-13,** The procedures described in Steps 8-10 were repeated for the Specify 5-6-5 paddle lead. Note that the intraoperative validation of the optimal position of the Specify 5-6-5 was restricted to one position to minimize the duration of the surgical intervention.

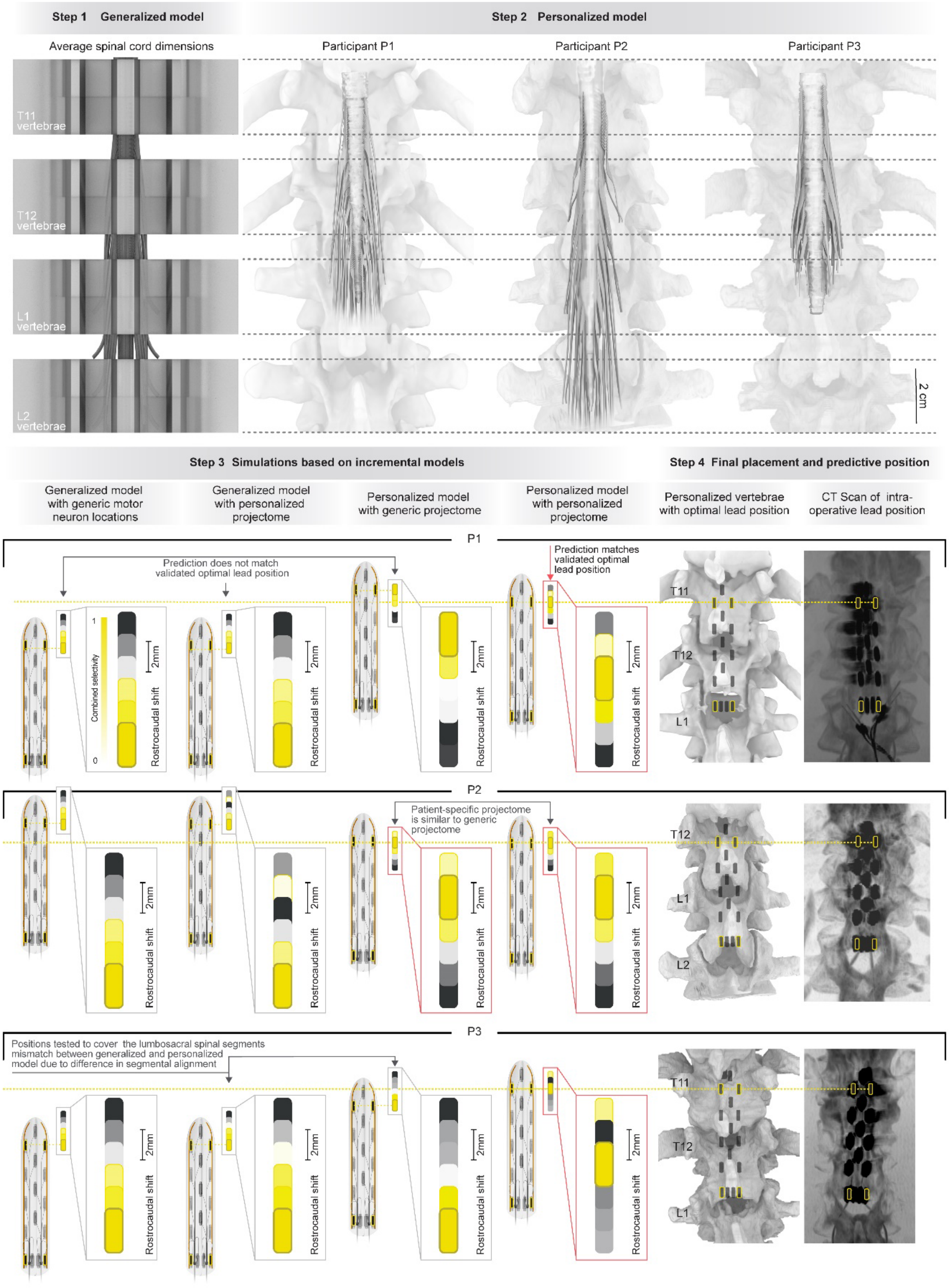

Extended Data Figure 5: Impact of model abstractions to determine the optimal position of the paddle lead. Step 1, Generalized computational model of the interaction between EES and the spinal cord, including the location of motor neurons from key leg muscles. **Step 2,** Personalized computational model of the interaction between EES and the spinal cord for the three participants. The models are aligned with the generalized model depicted in Step 1. **Step**

3, Simulations predict the optimal position of the new paddle lead for each participant, following the procedures explained in **Extended Data Figure 4**, but based on various model abstractions, as explained in the boxes above each prediction. **Step 4,** The optimal position of the new paddle lead was validated intraoperatively, as explained in **Extended Data Figure 4,** and is shown on a CT scan reconstruction. The horizontal yellow line passing through the top electrodes of the paddle lead highlights the optimal position, thus allowing a direct comparison between the various predictions and the optimal position. The fully personalized models achieved the best performance.

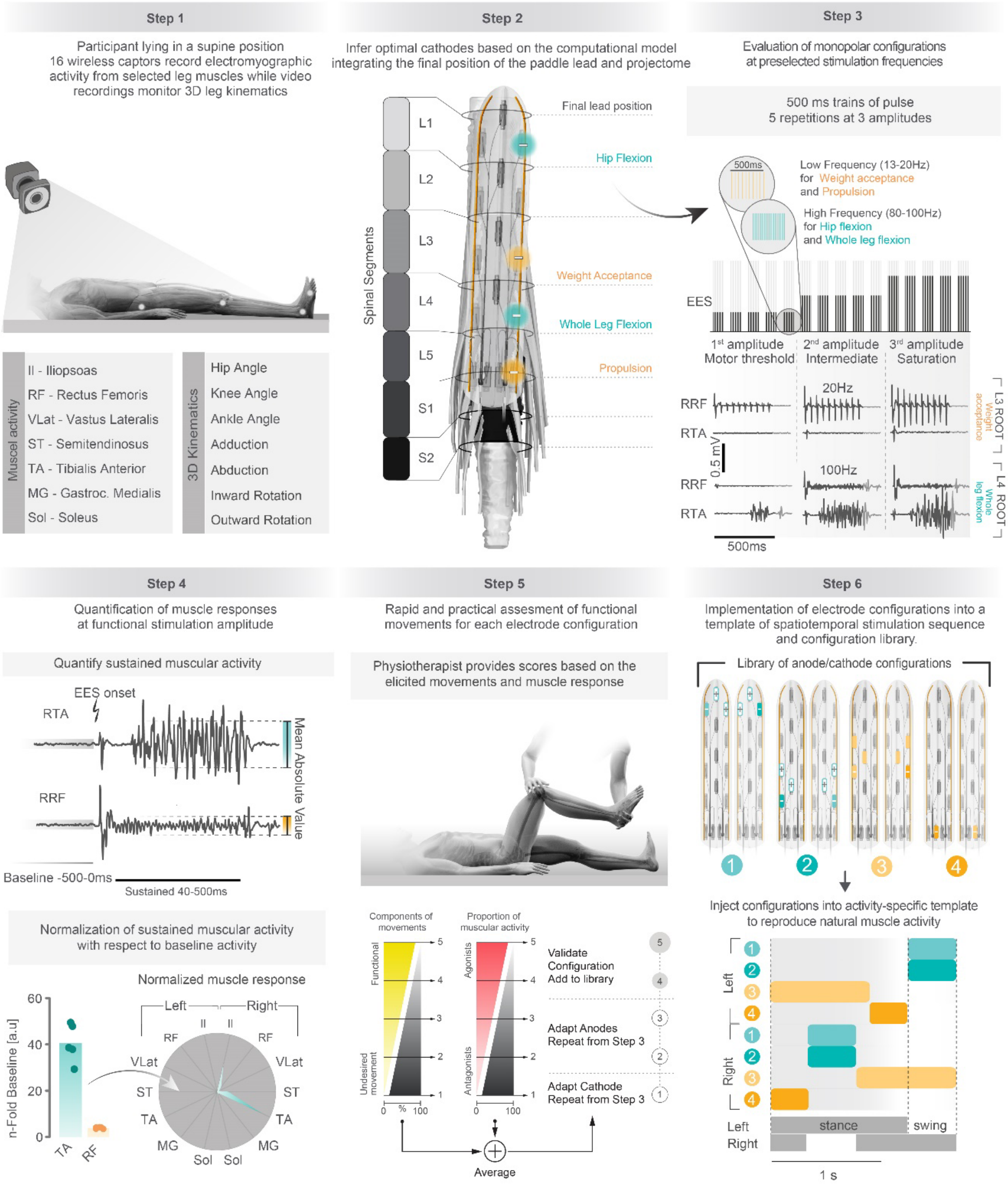

Extended Data Figure 6: Configuration of activity-specific stimulation protocols. Step 1, The participant is lying supine in a relaxed posture. Wireless sensors are positioned over selected leg muscles to monitor electromyographic signals in conjunction with leg kinematics using an optical 3D motion capture system. **Step 2,** Intraoperative imaging of the final paddle lead position guides the realignment of the paddle lead with respect to the personalized model of the interactions between EES and the spinal cord. The optimal cathode to target specific motor neurons are inferred based on the location of the electrodes with respect to the dorsal roots and location of motor neurons identified from fMRI measurements. **Step 3,** The performance of the preselected optimal cathode is assessed using trains of pulses delivered with predefined frequency ranges that are optimal for the targeted motor neurons. **Step 4,** The muscle responses are quantified from 40 to 500 ms after stimulation onset, and then normalized with respect to a baseline window selected 500ms before stimulation onset. The relative amplitudes of muscle responses are represented in a polar plot that allows to appreciate the relative recruitment of each muscle. **Step 5,** A physiotherapist grades the precision of the elicited movements and muscle activity based on a simple clinical scale that enables the quick adjustment of anode and cathode configurations to achieve the most optimal selectivity. **Step 6,** This procedure enables the rapid elaboration of a library of anode and cathodes targeting specific muscles and motor hotspots, which are then implemented in preprogrammed stimulation templates that aim to reproduce the natural activation of muscles during the desired activity.

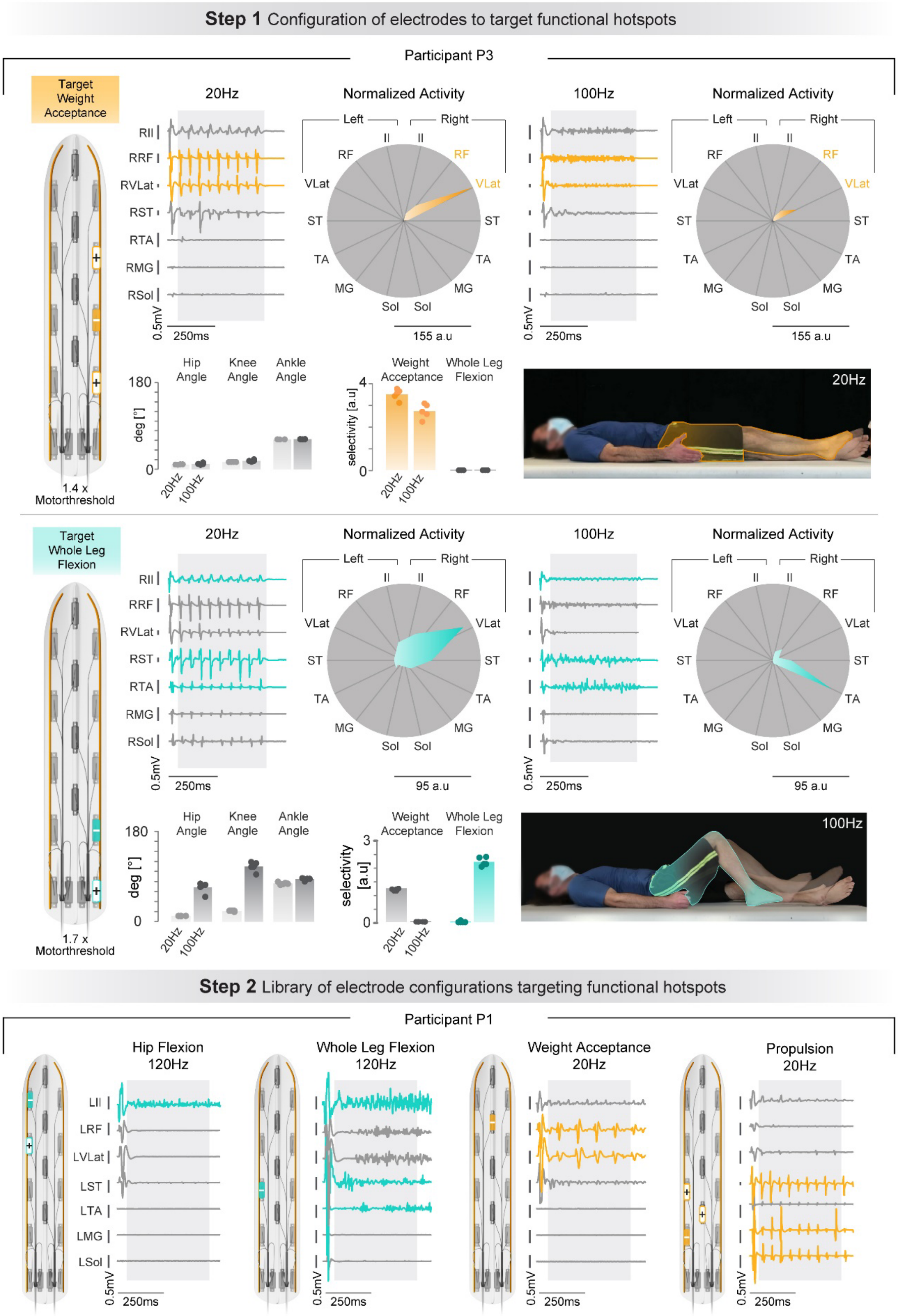

Extended Data Figure 7: Configurations of frequency-specific EES trains to elicit functional muscular and kinematic activity. Step 1, Configuration of electrodes to target the hotspots associated with weight acceptance (top) and whole-leg flexion (bottom). Example from participant P3. EES bursts are delivered at 20 Hz. (weight acceptance, optimal frequency for motor neurons innervating extensor muscles) and 100 Hz (whole-leg flexion, optimal frequency for motor neurons innervating flexor muscles) to elicit muscle responses, recorded from the Iliopsoas (*Il*), Rectus Femoris (*RF*), Vastus Lateralis (*VLat*), Semitendinosus (*ST*), Tibialis Anterior (*TA*), Gastrocnemius Medialis (*MG*), and Soleus (*Sol*) muscles (mean response, n=5 repetitions). The muscles associated with the targeted hotspot are color-coded. Polar plots report the normalized muscle responses, using the same convention as in **Extended Data Figure 7**. Polar plot units are normalized with respect to the baseline (n-fold). Bar plots report the amplitude of associated kinematic responses from each joint, and the selectivity indexes for targeted and non-targeted muscles (n=5 repetitions for each stimulation configuration). **Step 2**, Similar representations are shown for participant P1.

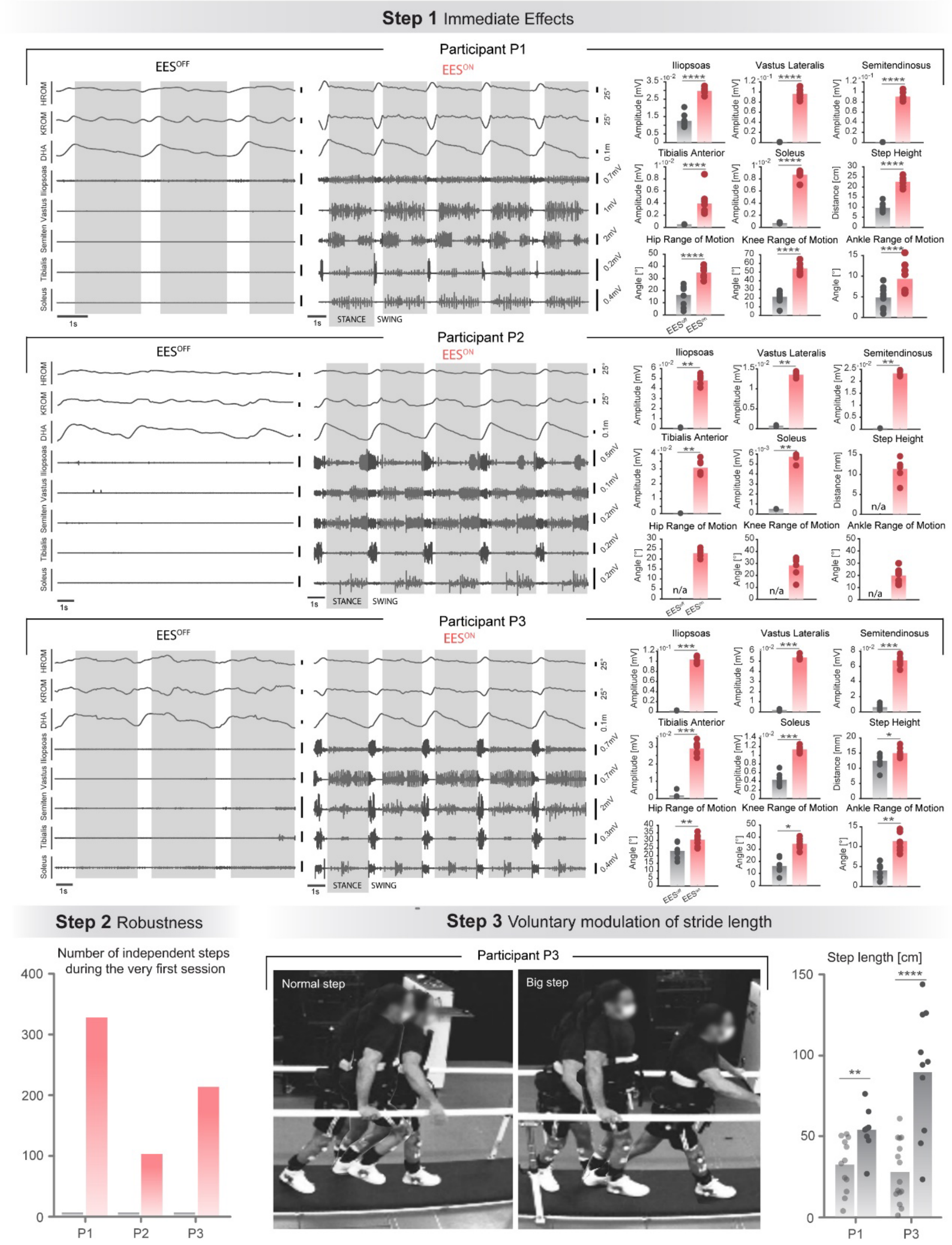

Extended Data Figure 8: Immediate recovery of independent stepping with EES. Step1, Kinematic and muscle activity underlying stepping on a treadmill without and with EES on the very first day of stimulation for the 3 participants. Bar plots report quantification of the muscle activity, and the range of motion for the hip, knee and ankle in both conditions (n=10 steps for each condition, two-tailed Mann-Whitney test, *, $p<0.05$; **, $p<0.01$; ***, $p<0.001$; ****, $p<0.0001$). Muscular activities are quantified as Mean Absolute Value over their expected phase of activity. **Step 2,** Number of independent steps performed during the very first day of stimulation. **Step 3,** Chronophotographies showing normal and voluntarily exaggerated steps while stimulation parameters remain otherwise unchanged. Bar plots report the mean step length quantified during normal and exaggerated steps (n=12 normal and 8 exaggerated steps for P1, n=15 normal and n=10 exaggerated steps for P2; two-tailed t-test, P1: $p=0.0073$, P3: $p<0.0001$; **, $p<0.01$; ****, $p<0.0001$).

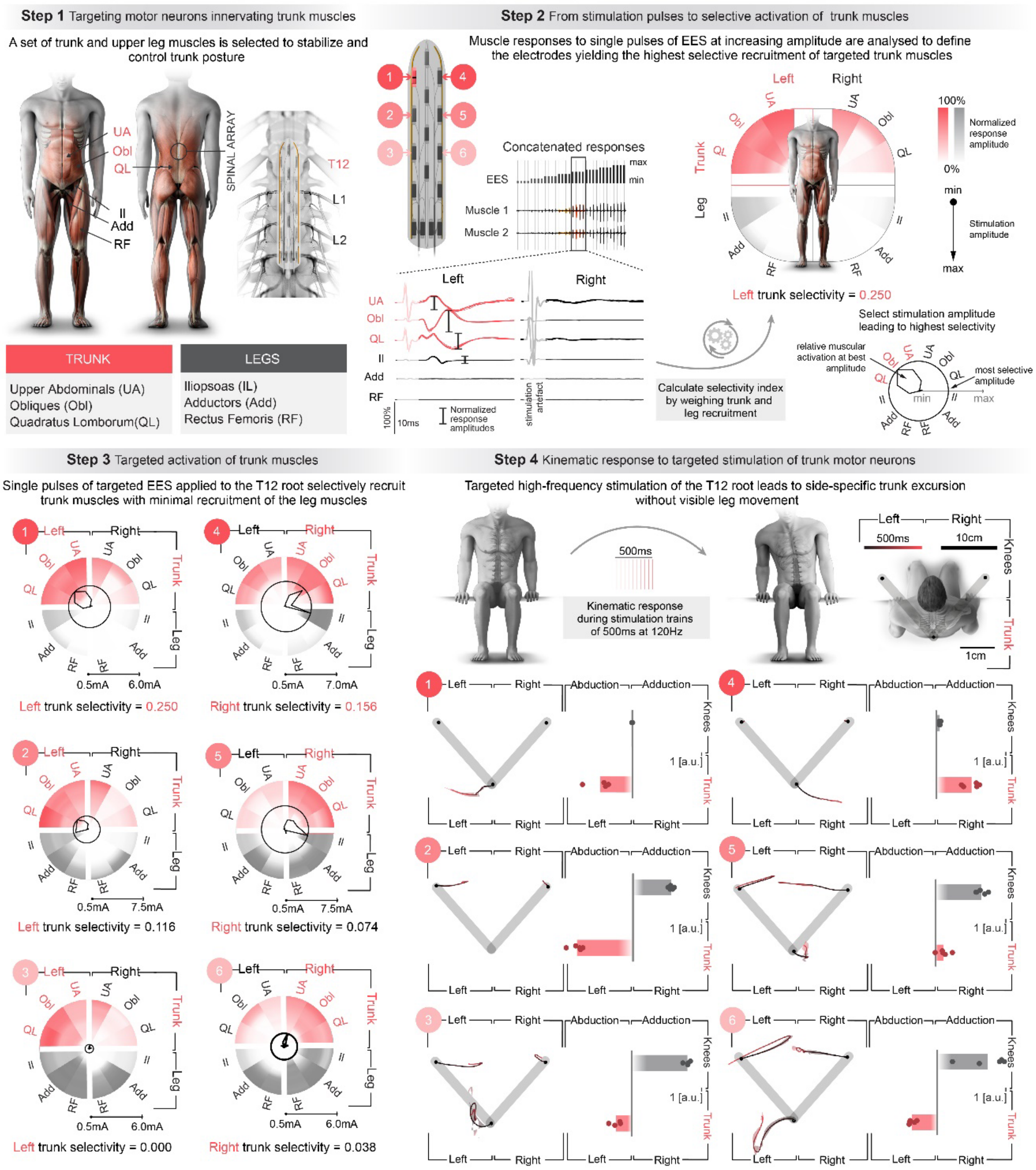

Extended Data Figure 9: Selective recruitment of trunk muscles. Step 1, Trunk and abdominal muscles are primarily innervated by motor neurons located in the thoracic region of the spinal cord. The new paddle array enables targeting the dorsal roots projecting to the T12 spinal segment, allowing the recruitment of trunk and abdominal muscles. **Step 2,** Single pulses of EES at increasing amplitude are delivered over electrodes to evaluate their ability to recruit trunk and abdominal muscles. Muscle responses are calculated, normalized, and then represented in a polar plot. The selectivity of trunk/abdominal versus leg muscle activation is calculated with a selectivity index formula. Side-specific recruitment of trunk and abdominal muscles is obtained with the upper electrodes of the new paddle lead. **Step 3,** Polar plots reporting the activation of trunk/abdominal muscles versus leg muscles when delivering EES through various electrodes of the new paddle lead, as indicated by the number referring to the electrodes depicted in step 2. **Step 4,** Trains of EES are delivered through the same electrodes as in Step 2 to elicit kinematic responses. For each tested electrode, the panels depict the mean time-dependent trajectory of trunk and knee movements in the plane perpendicular to the direction of gravity, and bar plots reporting the mean amplitude of trunk and knee movement in abduction or adduction. Electrodes 1 and 4, which are located over the top row of the new paddle lead, elicited side-specific trunk movement without disturbing knee movements.

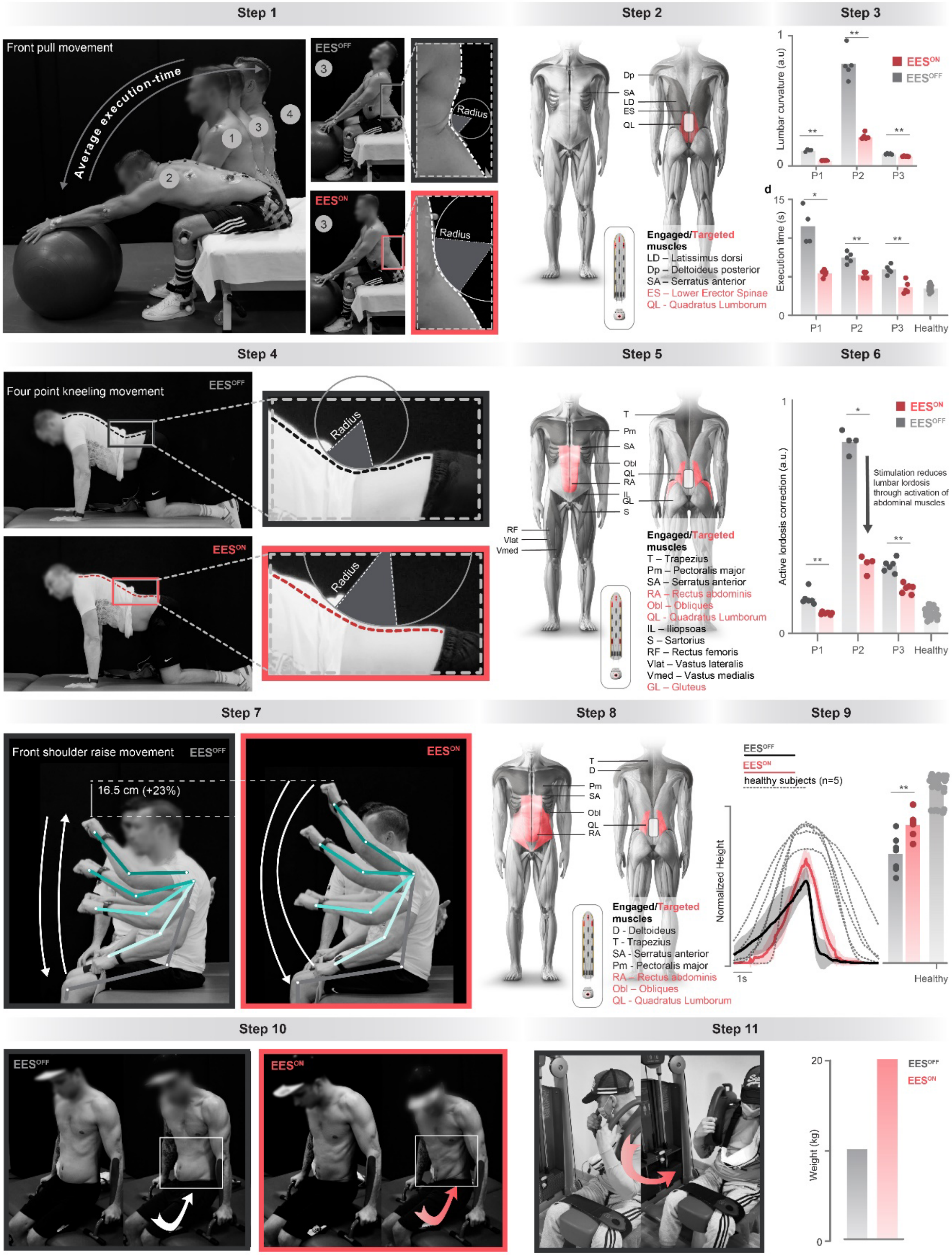

Extended Data Figure 10: Immediate recovery of trunk control. Step 1, Participant P2 performing repeated front pull movement on a medicine ball without stimulation (black/EES OFF) and with EES targeting the T12 dorsal root (red/EES ON). Radius of curvature of the lumbar region is measured at position 3, which is the most difficult position for the participants to stabilize. Exercises were repeated 4-5 times in each condition (EES OFF/ON). **Step 2,** Representation of the trunk muscles engaged in the execution of the task (grey) and EES targeted muscles (red), together with the electrode configuration to target the subset of these muscles affected by the SCI. **Step 3,** Bar plots reporting the radius of curvature of the lumbar region at position 3 and the execution time of the whole exercise for each participant (n=5 repetitions per participant, two-tailed Mann-Whitney test, Lumbar curvature (p=0.0079 for all three participants), Execution time (P1: p=0.0159, P2: p= 0.0079, P3: p=0.0079), *, p<0.05; **, p<0.01). **Step 4**, Participant P2 performing repeated lumbar lordosis correction in four-point kneeling position in the absence of stimulation (black /EES OFF) and with a stimulation program that targeted trunk, abdominal and gluteus muscles to stabilize the four-point kneeling position (red/EES ON). Radius of curvature of the lumbar region is measured at the time of maximal contraction and maximal relaxation of the lower back. Exercises were repeated 4-5 times in each condition (EES OFF/ON). **Step 5,** Same as Step 2. **Step 6**, Bar plots reporting the lumbar curvature without and with stimulation (n=6 (P1), n=4 (P2), n=6 (P3) repetitions, two-tailed Mann-Whitney test, P1: p=0.0022, P2: p=0.0286, P3: p=0.0022, *, p<0.05; **, p<0.01). **Step 7**, Participant P2 performing repeated front shoulder raise in the absence of stimulation (black/EES OFF) and with EES (red/EES ON). Exercises were repeated 4-5 times in each condition (EES OFF/ON). **Step 8,** Same as Step 2. **Step 9,** Changes in position of the wrist in the vertical plane during the front shoulder raise movement, showing improved symmetry and range of motion with EES turned on. The bar plot reports the execution time of this task with (n=7) and without EES (n=6), and in 5 healthy individuals for comparison (n=5 repetitions, two-tailed Mann-Whitney test, p=0.0082, **, p<0.01). **Step 10**, Dips lifting hip. In the absence of stimulation, the participant (P1) is able to lift his own body-weight but is not able to lift his pelvis (black). With EES, he is able to activate his lower abdominal and oblique muscles to lift his pelvis on both sides. **Step 11,** The participant (P1) is using a torso rotation machine at the gym. In the absence of stimulation, he is able to rotate to both sides lifting 10kg. EES enables him to perform this exercise with twice this weight as represented on the bar plot.

Methods

Study design and objectives

All experiments were carried out as part of the ongoing clinical feasibility study STIMO ("Stimulation Movement Overground"), which investigates the effects of spatiotemporal EES combined with weight-supported overground locomotor training on the recovery of motor function after SCI. This study was approved by the Swiss ethical authorities (Swissethics protocol number 04/2014 ProjectID: PB_2016-00886, Swissmedic protocol 2016-MD-0002) and was conducted in accordance with the Declaration of Helsinki. All participants signed a written informed consent prior to their participation. More information at clinicaltrials.gov (NCT02936453). All surgical and experimental procedures were performed at the Lausanne University Hospital (CHUV). The study involved assessments before surgery, the surgical implantation of the neurostimulation system, a one-month period during which EES protocols were configured, and a five-month rehabilitation period with physiotherapists taking place four to five times per week for one to three hours. The rehabilitation program was personalized based on the participants' improvements. At the end of the rehabilitation period, the participants were given the opportunity to be enrolled in a study extension phase during which they could continue using the neurostimulation system at home. They are currently followed-up on a regular basis by the study team for up to 6 years.

Study participants

Three individuals who had suffered a traumatic thoracic SCI participated in the study. Their neurological status was evaluated according to the International Standards for Neurological Classification of Spinal Cord Injury[1], and is reported in **Supplementary Data Table 1**. At the time of study enrollment, the following characteristics for the participants can be made: Participant P1 was 32 years old and was classified with a motor and sensory complete (AIS-A), T4 lesion that had occurred nine years earlier during a motor bike accident. He presented with bilateral leg paralysis, with motor scores of 0 on all key leg muscles. He could neither stand nor ambulate at all (WISCI score: 0), despite extensive participation in physical exercise with adapted devices for home use. Participant P2 was 41 years old and was classified with a motor and sensory complete (AIS-A) T6/T7 lesion that had occurred one year prior his enrollment during a motor bike accident. He presented with bilateral flaccid leg paralysis, with motor scores of 0 on all key leg muscles. He did not have any spasticity in his legs and could neither stand nor ambulate at all (WISCI score: 0), despite extensive participation in physical exercise with adapted devices for home use. Participant P3 was 29 years old, classified with a motor complete (AIS-B) T5/T6 lesion that had occurred three years earlier during a motor bike accident. He presented with bilateral spastic leg paralysis, with sensory and motor scores of 0 on all key leg muscles. He was classified as AIS-B due to the presence of deep anal pressure.

Cadaver analysis

The 12 cadavers samples were willingly given by donors to the anatomy department of the Centre Hospitalier Universitaire Vaudois (CHUV). Anthropometric measures on these samples complied with Swiss regulation on human studies and did not require formal approval. Formalin-fixated human spinal cords (n=12) were immersed in PBS 0,1M. The dura was carefully dissected using appropriate surgical tools to identify and expose the lumbo-sacral spinal segments. The roots were pinned individually using a specific color-code at their entry point to the cord. The length of each lumbo-sacral spinal segments was measured using a caliper. The length of each spinal segment was defined as the root attachment length plus the lower inter-root length. The measurements were averaged over the total number of dissected cords.

Imaging Data

Detailed methods for CT, structural MRI and functional MRI acquisitions are reported in **Supplementary Information**.

Mechanical vibration

MRI-compatible pneumatic vibrators were used to stimulate muscle spindle afferents. Small amplitude (0.5 mm peak to peak) and constant frequency (70 Hz) vibrations were delivered using a SMC ITV2050 air-pressure regulator driving the rotation of eccentric ceramic spherical masses embedded in the vibrator turbine. The stimulation parameters were selected based on the fact that small amplitude vibration activates preferentially primary muscle spindle endings, with responses linearly proportional to the vibration frequency up to 70-80 Hz[7]. A custom software implemented in the LabVIEW environment (National Instruments) allowed to synchronize the vibratory stimulations with the MRI acquisitions. This device did not produce artefacts in the fMRI scans, nor modified the signal-to-noise ratio, as already reported in previous studies during which vibrations were applied during brain fMRI acquisitions[8,9].

Six pneumatic vibrators were attached to the subject's right leg using elastic bands on the tendons of each pair of agonist/antagonist (extensor/flexor) muscles at the ankle, knee and hip levels. The aim was to target the Gastrocnemius Medialis/Soleus, Tibialis Anterior, Quadriceps, Iliopsoas, Gluteus and Biceps Femoris muscles. The protocol was divided in 2 runs for each pair of agonist/antagonist muscles per joint. In each run, two vibrators, one located on the flexor muscle and the other on the extensor muscle, were alternatively activated in blocks of 10 s. One run consisted of 18 alternate vibration blocks. To avoid any bias, the order of the 6 runs was randomized.

fMRI data Processing

The fMRI pre-processing was carried out using the FMRIB Software Library (FSL) v5.0.15 [10] and the Spinal Cord Toolbox (SCT) v4.3.16 [11].

A two-phase motion correction procedure was performed using FMRIB's Linear Image Registration Tool [12]. First, the volumes of each run were averaged into a mean image. The centerline of the spinal cord was automatically extracted [13]. A cylindrical mask of diameter 30 mm was drawn along it and used to exclude the regions outside the spinal cord. Within each run, all volumes were registered to the mean image using three-dimensional rigid body realignment (spline interpolation and least square cost function). To consider that the spinal cord is a non-rigid structure, a two-dimensional slice-wise realignment (spline interpolation and least square cost function) was conducted, taking as reference the mean image of the corrected volumes[14,15]. Finally, all runs corresponding to the same session in the scanner were aligned to the first run of the session using three-dimensional rigid body realignment (spline interpolation and least square cost function). All images were inspected to ensure that any artefacts or bottom slices with insufficient signal were cropped out. Two slices were in general removed per run. Motion scrubbing was also performed with FSL's tool to identify outliers volumes, using DVARS (the root mean square of the difference of intensity between consecutive volumes) metric in the spinal cord, with a box-plot cut-off (75th percentile + 1.5 x the interquartile range) [16].

Both the cerebrospinal fluid and the spinal cord were automatically segmented (with manual corrections when necessary) using the Spinal Cord Toolbox (SCT)[17] from the mean functional and the T2 anatomical images.

Nuisance regressors were built using FSL's physiological noise modelling tool on the acquired cardiac and respiratory signals, using an approach based on the RETROICOR procedure [18]. Low and high order Fourier expansions were used to model the physiological signals [19,20]. This resulted in 32 noise regressors, to which an additional cerebrospinal fluid regressor was included (10 % most variable cerebrospinal fluid voxels). When no physiological signals were available, regressors based on anatomical priors were determined using component-based noise extraction (aCompCor[21]) through the PhysIO Toolbox[22]. The motion corrected volumes were masked with the segmented cerebrospinal fluid mask. The first five principal components, as well as the mean of these time series were extracted and kept as noise regressors.

Coregistration was performed within each subject (functional-to-anatomical). Using the Spinal Cord Toolbox, functional images were coregistered to the T2 anatomical image with non-rigid transformations.

The motion corrected functional volumes were spatially smoothed, volume by volume, using a 3D Gaussian kernel (with full width half maximum (FWHM) of 2 x 2 x 6 mm3, along the centerline of the spinal cord, to preserve consistency at the anatomical level.

Spinal segments L1 to S2 were identified using the high-resolution structural MRI. The L1 dorsal root was identified from its entry region in the spinal canal (entering just below the L1 vertebra) until the region where it innervates the spinal cord, which defines the L1 spinal segment. The more caudal segments (L2 - S2) were identified by following the dorsal roots along the rostrocaudal axis.

fMRI data analysis

Using the pre-processed functional volumes (motion corrected, smoothed) and the noise regressors (physiological and motion outliers), for each run, a first-level statistical analysis was performed using FMRIB's Improved Linear Model with local auto-correlation correction [23]. As explanatory variables, the timings of the task (block design) were convolved with the three optimal basis functions using FMRIB's Linear Optimal Basis Set[24], with the second and third waveforms orthogonal to the first waveform. The resulting parameter estimates for the two runs were passed through a fixed-effects model to obtain the second level analysis (subject level and task specific) activation maps. To account for multiple comparisons, the Z statistic images were set to ($Z > 2$, $p < 0.05$) whenever possible. These results were then registered to the respective anatomical image to assess their spatial distribution with respect to spinal segments.

Personalized hybrid computational models

We designed a computational framework that supports the semi-automated creation of personalized, geometrically and neurofunctionally realistic hybrid neurophysical volume conductor models of the lower thoracic and lumbosacral spinal cord from high-resolution MRI and CT data. These models combine a 3D Finite Element Method (FEM) to characterize the electric potential and currents generated by EES with compartmental cable models to estimate the recruitment profile of individual nerve fibers. The detailed methods to generate these models and conduct simulations are reported in **Supplementary Information**.

Atlas of computational spinal cord models

Using our computational pipeline, we generated a freely available atlas of 15 personalized computational models from healthy volunteers. The models can be accessed at osparc.io/study/3c62d60a-319d-11ec-8033-02420a0b2de3. These models provided an instrumental resource to analyze the influence of electrode arrangements on the relative recruitment of dorsal roots. We also generated personalized computational models of our study participants. The models for the three participants can be accessed with the following links:

- Participant 1 : osparc.io/study/423e27aa-319d-11ec-8033-02420a0b2de3
- Participant 2: osparc.io/study/3f4ea128-319d-11ec-8033-02420a0b2de3
- Participant 3: osparc.io/study/389ac42e-319d-11ec-8033-02420a0b2de3

These models enabled precise preoperative planning that guided the neurosurgical procedure.

Neurosurgical intervention

Laminectomy and paddle lead insertion

An intraoperative tridimensional CT scan (O-Arm version 2, Medtronic, USA) was performed to map the predicted optimal position of the paddle leads to the anatomy of each participant, and thus guide the insertion of the leads at this position. An approximately 5 cm midline skin incision was performed, the fascia opened and the muscles retracted bilaterally. Excision of the midline ligamentous structures and laminectomy between L1 and L2 spinal segments enabled the insertion of the paddle leads that was placed over the midline of the exposed dura and advanced rostrally to the target location. Since the 5-6-5 Medtronic lead was narrower and shorter than the new paddle lead, this lead was inserted and tested first. This order minimized possible surgical complications due to the multiple entrances and trajectories within the spinal canal. After the neurophysiological evaluations, the paddle lead was secured by mean of bumpy anchors sutured to the ligaments, and a final 3D CT scan was then acquired to register the final position of the paddle lead.

Electrophysiological monitoring

Electrophysiological recordings were conducted using the NIM Eclipse monitoring and stimulation system (Medtronic Xomed Inc, Jacksonville, FL, USA). Single-pulses of EES (0.5 Hz) were delivered at increasing amplitude to elicit muscle responses that were recorded from subdermal (Neuroline Twisted Pair Subdermal, 12 x 0.4 mm, Ambu A/S, Ballerup, Denmark) or intramuscular needle electrodes (Ultra Sharp, 44 mm/27 g, Chalgren Enterprises, Inc. Gilroy, CA, USA).

Intraoperative comparison of the paddle leads

During the surgical intervention, the Specify 5-6-5 paddle lead (Specify 5-6-5, Medtronic Inc, Minneapolis, MN, USA) was inserted before the new paddle lead. Electrophysiological monitoring of muscle responses guided the placement to an optimal position to recruit the iliopsoas muscle (L1 dorsal root). Recordings were obtained at 3 different positions apart from

2 mm, centered around the optimal position. Then, the new paddle lead (Onward medical) was inserted through the same opening. The same procedure was then repeated. Since the new paddle lead displayed superior selectivity compared to the Specify 5-6-5, the new paddle lead was implanted chronically.

Paddle array

The new paddle array was fabricated using conventional biomedical technologies. Extensive bench and in vivo testing were conducted to validate the mechanical, electrical and biocompatibility properties of the paddle lead, which led to the equivalent of an investigational device exemption from Swiss competent authorities.

Pulse generator implantation

An implantable pulse generator (IPG) (Medtronic Activa™ RC, Medtronic Inc, Minneapolis, MN, USA) commonly used for Deep-Brain Stimulation therapies was inserted into a subcutaneous pocket in the participant's abdomen. The paddle array cables were then tunneled between both openings and connected to the implantable pulse generator.

Configuration of activity-specific stimulation programs

After approximately ten days of rest following the surgery, participants started a one-month period during which we configured activity-specific stimulation programs to support the performance of motor activities involving leg and trunk musculatures.

Electrode configurations

We delivered EES with electrode configurations targeting the dorsal roots projecting to the spinal cord regions containing the motor neuron pools associated with the intended movement- These spinal cord regions were derived from the projectome of proprioceptive neurons innervating the homonymous motor neurons, as identified with fMRI recordings. The cathodes were selected based on intraoperative recordings at the final position of the paddle lead. Additional anode configurations completed the cathodes to increase the selectivity when necessary. The procedure to elaborate the library of anodes and cathodes is described in **Extended Data Fig.6**. EES pulse width was fixed at 300µs. The amplitude and frequencies of EES were optimized for each electrode configuration, as described in **Extended Data Fig.7**.

Spatiotemporal stimulation sequences to support walking

Sequences of EES pulses to support walking were derived from the spatiotemporal maps of motor neuron activation reconstructed from muscle activity of healthy individuals during walking[36]. These spatiotemporal maps revealed that walking involves the successive activation of three hotpots restricted to specific spinal cord regions. We thus created a template of spatiotemporal stimulation sequences that aim to reproduce the spatiotemporal activation pattern of these hotspots during walking in healthy individuals. For each targeted hotspot, we selected an appropriate anode/cathode configuration from the library and updated the template with these configurations. The parameters (frequency, amplitude), onset and duration of each train of EES was optimized during walking on treadmill and overground and by inspecting the synchronicity of the muscular activity and kinematics with EES trains, and by integrating the feedback from the physical therapist and participant, as detailed in **Extended Data Fig.7**.

Spatiotemporal stimulation sequences to support other motor activities

We then configured activity-specific stimulation programs to support other motor activities such as standing, cycling, sit-to-stand, leg press and swimming. For this purpose, we exploited the same framework as for elaborating the stimulation template for walking. We thus conceived spatiotemporal sequences that reproduce the natural activation of motor hotpots / muscle groups during each motor activity. We also developed EES program that targeted the motor neurons innervating the trunk and abdominal musculatures to facilitate trunk postures and the execution of trunk exercises. This procedure is described in **Extended Data Fig.9**.

Clinical evaluations

International Standards for Neurological Classification of Spinal Cord Injury (ISNCSCI)

Participant's neurological status was assessed based on the ISNCSCI, a comprehensive clinician-administered neurological examination of residual sensory and motor function quantifying SCI severity[1].

Six-minute walk test

Endurance was assessed by the distance covered overground within 6 minutes with a standard 4-wheel walker and spatiotemporal EES turned on. This test was performed at the beginning and at the end of the 5-months of rehabilitation.

Quantification of muscle mass

Muscle mass was quantified from non-contrast CT images obtained with a 64-detector row CT scanner (Discovery CT750 HD, GE Healthcare) at the abdominal (L3 vertebra) and mid-thigh (25 cm cranial to the tibiofemoral joint space) levels, acquired prior to surgery and after the period of 5-month of rehabilitation. Muscle segmentations were performed semi-automatedly in ImageJ by applying specific CT number thresholds (in Hounsfield unit, HU) for the identification of muscle (from -29 to +150 HU) and adipose (from -190 to -30 HU) tissues[37]. Muscle mass and skeletal muscle area are reported in cm^2 for specific abdominal and thigh muscles or muscle compartments.

Rehabilitation program

Participants followed a rehabilitation program four to five times per week for five months. The rehabilitation program was personalized to participants' performance. This period of rehabilitation comprised walking on a treadmill and overground with multiple assistive devices, sit-to-stand, standing, leg and trunk muscle exercises, swimming and cycling. Activity-specific stimulation programs were delivered to enable the practice of these activities.

Technological framework

Rehabilitation and movement analysis environment

When necessary, a tailored amount of body weight support was provided to the participants using an overhead support system based on cable robot technology (Rysen, Motek Medical BV). This robotic system allows the application of tailored forces to the trunk through a dedicated harness along the vertical and anteroposterior directions.

Electromyographic activity of selected muscles was acquired at a 2kHz sample rate using the 16-channel wireless Delsys system, with bipolar surface electrodes placed over the following muscles of the lower limbs (iliopsoas (Il), rectus femoris (RF), adductors (Add), vastus lateralis (VLat), semitendinosus (ST), tibialis anterior (TA), medial gastrocnemius (MG), and soleus (Sol)) and/or trunk muscles (Abdominal Muscles (Abs), Quadratus Lomborum (QL) and Obliques (Obl)). Kinematic recordings were obtained at a 100-Hz sampling rate using a 3D motion capture system (Vicon Motion Systems, Oxford, UK and Nexus v1.8.5 software), consisting of 14 infrared cameras that covered a 12 x 4 x 2.5 m workspace. Body kinematics were captured by these infrared cameras through the use of infrared-reflective markers positioned over standardized anatomical landmarks. We also captured chronophotographic images of participants using a high-definition camera (FUJIFILM X-T2, 5 images/s, ISO 6400, shutter speed 1/250 sec). Successive snapshots were overlaid offline to illustrate the dynamic of movements.

Neurostimulation system

EES was delivered with an implantable pulse generator (IPG, Medtronic Activa™ RC) that enabled monopolar and multipolar stimulation at constant current or constant voltage through one or a subset of the 16 electrodes of the paddle lead or the case of the IPG (anode). The IPG was modified from its clinical version with an investigational firmware that enabled real-time communication with a software running on an external computer (NEUWalk Research Programmer Application or NRPA, Model 09103, Medtronic). The NRPA acted as a relay between EES triggering commands sent by the control software called G-Drive Plus (described below) and the IPG. The NRPA communicated wirelessly with the IPG through the following communication chain: the NRPA sent commands via a virtual COM port corresponding to a Bluetooth adapter, a custom wireless bridge consisting of a nano computer (Raspberry Pi) received this command and forwarded it to a virtual COM port 6 corresponding to a USB adapter, a USB to infrared adapter (ACT-IR224UN-LN115-LE, ACTiSYS Corporation, Fremont, CA, USA) transformed this command into infrared signals that were then read by a modified Medtronic patient's programmer (Sensing Programmer Telemetry Module SPTM, Medtronic), which finally transmitted the command to the patient's IPG by electromagnetic induction through the skin (**Supplementary Fig. 1**).

Software App for configuration, optimization and evaluation of neurostimulation

A custom software App was built to configure, optimize and evaluate the effects of EES (See **Supplementary Information**). The C# App runs on a desktop computer, laptop or tablet and interfaces with the stimulation system (through the NRPA application) and sensor systems for data acquisition and closed-loop stimulation. The software includes a stimulation scheduler that enables the rapid personalization of spatiotemporal stimulation sequences from preprogrammed templates. The user can choose to loop a sequence automatically, to switch between different motor activities with one click, or to link stimulation sequences to specific events detected by the sensors. These events can be triggered by detecting movement-specific changes detected through inertial measurement units (IMUs) (NGIMU, x-io Technologies Limited) placed on the participant's body or by clicking on custom-built ergonomic buttons mounted on an assistive device and connected to the analog input ports of the IMUs. The IMUs are connected with the software App through Wifi, streaming quaternion or analog input data at 30Hz. For movement detection, quaternion values are converted into Euler angles indicating the angular positions of the trunk or limbs, depending on the location of the IMUs. Movement-specific events are triggered when these angles cross user-defined and movement-specific thresholds in a predefined direction. The software provides real-time visualization (SciChart WPF library, SciChart Ltd) of the muscular activity and leg kinematics based on wireless sensors that measures the electromyographic activity and inertial measurement units placed on the participant's body (Delsys Trigno system, Delsys

Incorporated). The App also triggers acquisition from video cameras. The muscular and kinematic data are synchronized with the stimulation sequences and color-coded with respect to the targeted motor hotspots. This color-coded visualization allows the immediate assessment of the effects of the stimulation on muscle activity and whole-body kinematics. All the acquired data, including the information about EES stimulation patterns, are saved for offline analysis.

The App provides graphical interfaces tailored to the needs of the different user types, i.e. stimulation experts, physical therapists and study participants. Concretely, the same App can be used by stimulation experts on a multi-screen desktop system to configure and optimize stimulation parameters, by therapists to select and modulate rehabilitation exercises on a handheld tablet, or by study participants to start and stop activity-dependent stimulation programs to support activities of daily living through a smartwatch.

Data processing

Analysis of intraoperative muscle activity

Intraoperative recordings of muscle activity were band-pass filtered between 10 and 450 Hz (4th-order Butterworth filter). The peak-to-peak amplitudes of the monosynaptic components of muscle responses were extracted and normalized with respect to the maximal value obtained during the recordings.

Analysis of lower limb muscle activity

The electromyographic activity from lower limb muscles was processed according to the SENIAM (Surface Electromyography for the Non-Invasive Assessment of Muscles) standards for electromyographic recordings. All displayed electromyographic activities during walking were band-pass filtered between 10 and 450 Hz (4th -order Butterworth filter). A moving average of the rectified electromyographic signal within a centered 250-ms time window was used to generate normalized electromyographic envelopes for quantification.

Recruitment of trunk and abdominal muscles during single-pulse EES

Electromyographic signals from trunk abdominal muscles were band-passed filtered between 10 and 450 Hz (4th -order Butterworth filter. EES onset was determined using semi-automatic methods based on recordings of stimulation artefacts. The temporal window of muscle responses was defined within a 40 or 50 ms starting 10 ms after EES onset, depending on the muscle. For each amplitude of EES, muscle responses were quantified as the peak-to-peak amplitude. These values were translated into recruitment curves that we displayed in circular plots. In these circular plots, muscles are distributed at different angular positions. The radial axis corresponds to EES amplitude (**Extended Data Fig. 8**). A color shading reports the normalized amplitude of muscle activity. The black circle highlights the EES amplitude that corresponds to the highest selectivity index. The polygon describes the muscle selectivity at the optimal EES amplitude: the edges of the polygon represent the normalized muscle activity on the radial axis for a particular muscle, scaled so that the polygon fills the circle.

Analysis of trunk kinematics

Reflective markers were secured to the spine at T10 and L5, and on both knees to record trunk and leg kinematics. The responses were analyzed over the window of 500ms that followed the onset of the stimulation. Kinematic data was low-pass filtered (4th-order Butterworth filter) with a cut-off at 10Hz.

Analysis of trunk posture and kinematics during exercises
Trunk exercises were recorded with a FujiFilm XT-2 camera. Video-based kinematic analysis of the lumbar curvature was performed through a semi-automated detection of the body segments and by an expert visually fitting circles to calculate the lumbar curvature.

Statistics

All quantifications show the mean and all individual data. Comparisons between two conditions were performed using a two-tailed Student's t-test, when normality was confirmed or a non-parametric Mann-Whitney rank sum test otherwise. Comparisons involving more than two categories were performed using a 1-way ANOVA, followed by the post-hoc Tukey's Honest Significance Difference tests. *, **, *** indicate a p-value smaller than 0.05, 0.01, 0.001 respectively.

Data Availability

Data that supports the findings are available in the following data depository:
https://doi.org/10.5281/zenodo.5614586
Main figures (Fig 1-6) and extended data figures (Ext.Fig 2-10) have associated raw data.

Code Availability

Software routines developed for the data analysis will be made available upon reasonable request to gregoire.courtine@epfl.ch.

Acknowledgements

We thank our study participants for their commitment and trust. Participants have given their informed consent for publication of their images.; Dr. Armin Curt for support; Anja van der Kolk and Fredy Visser for support in imaging data collection and inspection; Many students, interns and former employees for various contributions: Ruijia Wang, Corentin Puffay, Yeuk Ling Ricky Wan, Ivan Perret, Emilie Revol, Marine Van Campenhoudt, Ibrahim Youssef, Ionut Turcu, Flavien Sellet, Gaia Carparelli, Charlotte Moerman, Deborah Scherrer-Ma, Fanny Magaud, Matilde Damiani, Nicola Regazzi; Investigational implantable stimulators and paddle leads were donated from Medtronic and Onward Medical.

References for the Methods section

1. Kirshblum, S. & Waring, W. Updates for the International Standards for Neurological Classification of Spinal Cord Injury. *Phys Med Rehabil Cli* **25**, 505–517 (2014).

2. Weber, K. A. *et al.* Assessing the spatial distribution of cervical spinal cord activity during tactile stimulation of the upper extremity in humans with functional magnetic resonance imaging. *Neuroimage* **217**, 116905 (2020).

3. Kinany, N., Pirondini, E., Micera, S. & Ville, D. V. D. Dynamic Functional Connectivity of Resting-State Spinal Cord fMRI Reveals Fine-Grained Intrinsic Architecture. *Neuron* **108**, 424-435.e4 (2020).

4. Kinany, N. *et al.* Functional imaging of rostrocaudal spinal activity during upper limb motor tasks. *Neuroimage* **200**, 590–600 (2019).

5. Weber, K. A., Chen, Y., Wang, X., Kahnt, T. & Parrish, T. B. Functional magnetic resonance imaging of the cervical spinal cord during thermal stimulation across consecutive runs. *Neuroimage* **143**, 267–279 (2016).

6. Weber, K. A., Chen, Y., Wang, X., Kahnt, T. & Parrish, T. B. Lateralization of cervical spinal cord activity during an isometric upper extremity motor task with functional magnetic resonance imaging. *Neuroimage* **125**, 233–243 (2016).

7. Roll, J. P. & Vedel, J. P. Kinaesthetic role of muscle afferents in man, studied by tendon vibration and microneurography. *Exp Brain Res* **47**, 177–190 (1982).

8. Landelle, C., Ahmadi, A. E. & Kavounoudias, A. Age-Related Impairment of Hand Movement Perception Based on Muscle Proprioception and Touch. *Neuroscience* **381**, 91–104 (2018).

9. Kavounoudias, A. *et al.* Proprio-tactile integration for kinesthetic perception: An fMRI study. *Neuropsychologia* **46**, 567–575 (2008).

10. Jenkinson, M., Beckmann, C. F., Behrens, T. E. J., Woolrich, M. W. & Smith, S. M. FSL. *Neuroimage* **62**, 782–790 (2012).

11. Leener, B. D. *et al.* SCT: Spinal Cord Toolbox, an open-source software for processing spinal cord MRI data. *Neuroimage* **145**, 24–43 (2017).

12. Jenkinson, M., Bannister, P., Brady, M. & Smith, S. Improved Optimization for the Robust and Accurate Linear Registration and Motion Correction of Brain Images. *Neuroimage* **17**, 825–841 (2002).

13. Gros, C. *et al.* Automatic spinal cord localization, robust to MRI contrasts using global curve optimization. *Med Image Anal* **44**, 215–227 (2018).

14. K., W., C.Y., I., X., W. & T., P. Choice of motion correction method affects spinal cord fMRI results. in *20th Annual Meeting of the Organization for Human Brain Mapping* (2014).

15. Cohen-Adad, J. *et al.* Venous effect in spinal cord fMRI: insights from intrinsic optical imaging and laser speckle. *Neuroimage* **47**, S186 (2009).

16. Power, J. D. *et al.* Methods to detect, characterize, and remove motion artifact in resting state fMRI. *Neuroimage* **84**, 320–341 (2014).

17. Gros, C. *et al.* Automatic segmentation of the spinal cord and intramedullary multiple sclerosis lesions with convolutional neural networks. *Neuroimage* **184**, 901–915 (2019).

18. Eippert, F., Kong, Y., Jenkinson, M., Tracey, I. & Brooks, J. C. W. Denoising spinal cord fMRI data: Approaches to acquisition and analysis. *Neuroimage* **154**, 255–266 (2017).

19. Brooks, J. C. W. *et al.* Physiological noise modelling for spinal functional magnetic resonance imaging studies. *Neuroimage* **39**, 680–692 (2008).

20. Kong, Y., Jenkinson, M., Andersson, J., Tracey, I. & Brooks, J. C. W. Assessment of physiological noise modelling methods for functional imaging of the spinal cord. *Neuroimage* **60**, 1538–1549 (2012).

21. Behzadi, Y., Restom, K., Liau, J. & Liu, T. T. A component based noise correction method (CompCor) for BOLD and perfusion based fMRI. *Neuroimage* **37**, 90–101 (2007).

22. Kasper, L. *et al.* The PhysIO Toolbox for Modeling Physiological Noise in fMRI Data. *J Neurosci Meth* **276**, 56–72 (2017).

23. Woolrich, M. W., Ripley, B. D., Brady, M. & Smith, S. M. Temporal Autocorrelation in Univariate Linear Modeling of FMRI Data. *Neuroimage* **14**, 1370–1386 (2001).

24. Woolrich, M. W., Behrens, T. E. J. & Smith, S. M. Constrained linear basis sets for HRF modelling using Variational Bayes. *Neuroimage* **21**, 1748–1761 (2004).

25. Krcah, M., Szekely, G. & Blanc, R. Fully Automatic and Fast Segmentation of the Femur Bone from 3D-CT Images with No Shape Prior. *2011 Ieee Int Symposium Biomed Imaging Nano Macro* 2087–2090 (2011) doi:10.1109/isbi.2011.5872823.

26. Akkın, S. M. Atlas of the Spinal Cord of the Rat, Mouse, Marmoset, Rhesus and Human by Gulgun Sengul, Charles Watson, Ikuko Tanaka and George Paxinos. *Anat* **7**, 68–68 (2015).

27. Neufeld, E., Szczerba, D., Chavannes, N. & Kuster, N. A novel medical image data-based multi-physics simulation platform for computational life sciences. *Interface Focus* **3**, 20120058 (2013).

28. Liu, Y., Zhou, X., Ma, J., Ge, Y. & Cao, X. The diameters and number of nerve fibers in spinal nerve roots. *J Spinal Cord Medicine* **38**, 532–537 (2014).

29. Capogrosso, M. *et al.* A Computational Model for Epidural Electrical Stimulation of Spinal Sensorimotor Circuits. *J Neurosci* **33**, 19326–19340 (2013).

30. Ladenbauer, J., Minassian, K., Hofstoetter, U. S., Dimitrijevic, M. R. & Rattay, F. Stimulation of the Human Lumbar Spinal Cord with Implanted and Surface Electrodes: A Computer Simulation Study. *Ieee T Neur Sys Reh* **18**, 637–645 (2010).

31. Hines, M. L. & Carnevale, N. T. Neuron: A Tool for Neuroscientists. *Neurosci* **7**, 123–135 (2001).

32. Gaines, J. L., Finn, K. E., Slopsema, J. P., Heyboer, L. A. & Polasek, K. H. A model of motor and sensory axon activation in the median nerve using surface electrical stimulation. *J Comput Neurosci* **45**, 29–43 (2018).

33. D., S., J.T., M. & D., D. Modeling of mammalian myelinated nerve for functional neuromuscular stimulation. in *IEEE/Engineering in Medicine and Biology Society Annual Conference* (IEEE, 1987).

34. Sundt, D., Gamper, N. & Jaffe, D. B. Spike propagation through the dorsal root ganglia in an unmyelinated sensory neuron: a modeling study. *J Neurophysiol* **114**, 3140–3153 (2015).

35. Schirmer, C. M. *et al.* Heuristic map of myotomal innervation in humans using direct intraoperative nerve root stimulation: Clinical article. *J Neurosurg Spine* **15**, 64–70 (2011).

36. Wagner, F. B. *et al.* Targeted neurotechnology restores walking in humans with spinal cord injury. *Nature* **563**, 65–71 (2018).

37. Gomez-Perez, S. L. *et al.* Measuring Abdominal Circumference and Skeletal Muscle From a Single Cross-Sectional Computed Tomography Image. *Jpen-parenter Enter* **40**, 308–318 (2016)

Participant	P1		P2		P3	
Gender	m		m		m	
Age at study enrolment (y)	32		41		29	
Years after SCI at study enrolment	8 years and 11 months		1 year and 3 months		2 years and 10 months	
Assessment at study enrolment (Pre) and after rehabilitation period (Post)	Pre	Post	Pre	Post	Pre	Post
American Spinal Injury Association Impairment Scale (AIS)	A	A	A	A	B	C
Neurological level of injury	T4	T3	T3	T3	T7	T7
Lower Extremity Motor Score						
L2, hip flexors (right | left)	0 | 0	0 | 0	0 | 0	0 | 0	0 | 0	1 | 2
L3, knee extensors (right | left)	0 | 0	0 | 0	0 | 0	0 | 0	0 | 0	1 | 1
L4, ankle dorsiflexors (right | left)	0 | 0	0 | 0	0 | 0	0 | 0	0 | 0	0 | 1
L5, long toe extensors (right | left)	0 | 0	0 | 0	0 | 0	0 | 0	0 | 0	0 | 0
S1, ankle plantar flexors (right | left) (max. 5 per side)	0 | 0	0 | 0	0 | 0	0 | 0	0 | 0	0 | 0
Total (max. 25 | 25)	0 | 0	0 | 0	0 | 0	0 | 0	0 | 0	2 | 4
Deep anal pressure (DAP)	No	No	No	No	Yes	Yes
Voluntary anal contraction (VAC)	No	No	No	No	No	No
Light-Touch Sensory score						
L1-S2 dermatomes subscore (right | left)	0 | 0	0 | 0	0 | 0	0 | 0	0 | 0	0 | 0
Total (max. 112)	23 | 23	22 | 22	23 | 23	21 | 22	32 | 31	30 | 31
Pin Prick Sensory Scores						
L1-S2 dermatomes subscore (right | left)	0 | 0	0 | 0	0 | 0	0 | 0	0 | 0	0 | 0
Total (max. 56 | 56)	22 | 22	21 | 22	24 | 24	21 | 21	30 | 28	30 | 30

Supplementary Data Table 1 : Demographic and neurological status of participants

Supplementary information

Supplementary Figure 1: software for configuration, optimisation, evaluation and implementation of activity. Step 1, A custom-built software named GDrive+ integrates signals from video cameras, sensors of muscle activity, and inertial measurement units (accelerometers and gyroscopes) in real-time and wirelessly. Each configuration of electrodes targeting a given hotspot/muscle group is color-coded in the interface, and is visualized onto the kinematic and physiological signals when EES is turned on. This synchronized visualization provides direct feedback to configure and optimize activity-specific stimulation programs. This configuration is performed via dedicated graphical interfaces that allow to change the timing and parameters of stimulation directly onto a stimulation scheduler and ergonomic windows, including touch screens. This software allows the configuration and personalization of activity-dependent stimulation programs in less than one hour. **Step 2,** EES commands are transmitted to the implantable pulse generator (IPG) via Bluetooth (1) to a module that converts them into infrared signals (2), which are then transferred to the stimulation programmer device (2′). The stimulation programmer transmits EES commands into the IPG via induction telemetry (4), using an antenna (3) taped to the skin and aligned to the IPG. EES is delivered through the paddle array (5). This communication chain allows the control of up to 4 concomitant stimulation waveforms in real-time, with a response latency of approximately 120 ms. **Step 3,** A handheld tablet and connected smartwatch (1) running our custom-made software App provide user-friendly interfaces for therapists and participants to select activity-specific stimulation programs (2) and to adapt relevant stimulation parameters of these programs (3) to perform rehabilitation exercises or support activities of daily living. Custom-built ergonomic clickers (4) or inertial measurement units (5) are placed on the body or assistive devices to ensure that the stimulation is delivered with a timing corresponding to the intended movement.

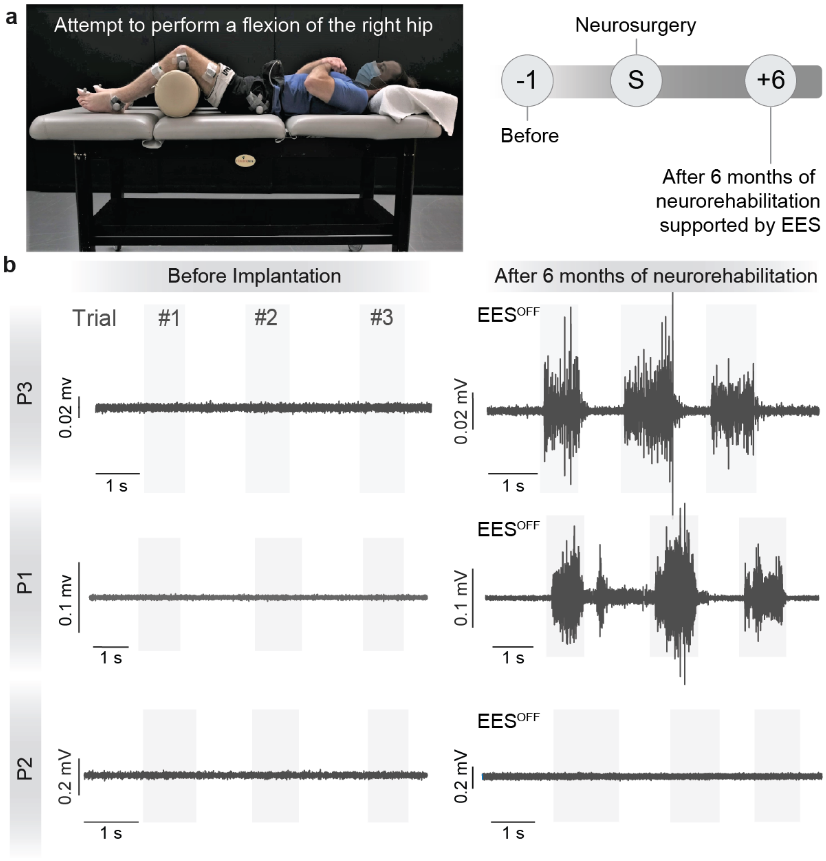

Supplementary Figure 2: Volitional activation of muscles. a, While lying in a supine position, participants were requested to attempt to perform three successive flexions of the right hip without EES and in the absence of any facilitation manoeuvres. Data is shown before the neurosurgical implantation and after 6 months of neurorehabilitation supported by EES. **b,** EMG activity was recorded from the right Iliopsoas. Two out of 3 participants with complete sensorimotor paralysis recovered volitional activation of the Iliopsoas muscle with EES turned off.

Participant	P1		P2		P3	
Gender	m		m		m	
Age at study enrolment (y)	32		41		29	
Years after SCI at study enrolment	8 years and 11 months		1 year and 3 months		2 years and 10 months	
Assessment at study enrolment (Pre) and after rehabilitation period (Post)	Pre	Post	Pre	Post	Pre	Post
American Spinal Injury Association Impairment Scale (AIS)	A	A	A	A	B	C
Neurological level of injury	T4	T3	T3	T3	T7	T7
Lower Extremity Motor Score						
L2, hip flexors (right | left)	0 | 0	0 | 0	0 | 0	0 | 0	0 | 0	1 | 2
L3, knee extensors (right | left)	0 | 0	0 | 0	0 | 0	0 | 0	0 | 0	1 | 1
L4, ankle dorsiflexors (right | left)	0 | 0	0 | 0	0 | 0	0 | 0	0 | 0	0 | 1
L5, long toe extensors (right | left)	0 | 0	0 | 0	0 | 0	0 | 0	0 | 0	0 | 0
S1, ankle plantar flexors (right | left) (max. 5 per side)	0 | 0	0 | 0	0 | 0	0 | 0	0 | 0	0 | 0
Total (max. 25 | 25)	0 | 0	0 | 0	0 | 0	0 | 0	0 | 0	2 | 4
Deep anal pressure (DAP)	No	No	No	No	Yes	Yes
Voluntary anal contraction (VAC)	No	No	No	No	No	No
Light-Touch Sensory score						
L1-S2 dermatomes subscore (right | left)	0 | 0	0 | 0	0 | 0	0 | 0	0 | 0	0 | 0
Total (max. 112)	23 | 23	22 | 22	23 | 23	21 | 22	32 | 31	30 | 31
Pin Prick Sensory Scores						
L1-S2 dermatomes subscore (right | left)	0 | 0	0 | 0	0 | 0	0 | 0	0 | 0	0 | 0
Total (max. 56 | 56)	22 | 22	21 | 22	24 | 24	21 | 21	30 | 28	30 | 30

Supplementary Data Table 1 : Demographic and neurological status of participants

SUPPLEMENTARY METHODS

Healthy volunteer MRI Data

Healthy volunteers were recruited via local advertisements. Study information were therefore given by direct communications and by means of information letters. Only subjects meeting the inclusion criteria were included. The MRI study on healthy volunteers was approved by the local medical research ethics committee (METC) of the UMC Utrecht and was conducted according to the principles of the Declaration of Helsinki. 15 healthy volunteers, including 7 males and 8 females, participated in the MRI study. The mean age of the population was 29±5. Mean anthropometric values are as follows. Height: 1.78±0.13 Weight: 76.7±18.5 BMI: 23.9±4.5**.** MRI acquisitions on these healthy volunteers were performed on a 3T Philips Ingenia system (Philips Healthcare, Best, The Netherlands) in supine position. For these acquisitions, we used the torso anterior receiver coil and the posterior receiver coil (embedded in the MRI table). The following sequences were acquired:

- T2-weighted MRI sequence; Multi-Slice Cartesian fast-field-echo (FFE); field-of-view (anterior-posterior/feet-head/ right-left): 180x480x92 mm3; acquired resolution: 1x1x3 mm3; reconstructed resolution: 0.75x0.75x3 mm3; slice orientation: sagittal; repetition time/echo time: 334/8.1 ms; flip angle: 25; number of signal averages: 3; acquisition time: 5 min 20 sec.
- T1-weighted MRI sequence; Multi-Slice Cartesian fast-field-echo (FFE); field-of-view (anterior-posterior/feet-head/ right-left): 180x480x92 mm3; acquired resolution: 1x1x3 mm3; reconstructed resolution: 0.75x0.75x3 mm3; slice orientation: sagittal; repetition time/echo time: 140/4.6 ms; flip angle: 80; number of signal averages: 2; acquisition time: 5 min 20 sec.
- Gray/white matter contract (butterfly) sequence; Multi-Slice Multi-Echo Cartesian fast-field-echo (FFE); field-of-view (anterior-posterior/feet-head/ right-left): 80x135x200 mm3; acquired resolution: 0.8x0.8x4 mm3; reconstructed resolution: 0.5x0.5x4 mm3; slice orientation: transverse; repetition time/echo time/delta echo time: 993/4.6/6.1 ms; Number of echoes = 4; flip angle: 65; number of signal averages: 1; acquisition time: 5 min 15 sec.
- A 3D fast-field-echo (FFE) balanced-steady-state-free-precession sequence (bSSFP) was developed to visualize the nerve roots inside the spinal canal. This sequence is T1/T2*-weighted, thus the nerve roots appear with negative contrast against cerebrospinal fluid (CSF). It has an almost isotropic resolution allowing multiplanar-reconstruction (MPR) with negligible loss of details. Furthermore, it is fully balanced, thus allowing high SNR, and intrinsically flow compensated. Hence, CSF flow artifacts affecting standard clinical sequences are minimized. The following imaging parameters were used: field-of-view (right-left/anterior-posterior/feet-head): 250x40x350 mm^3; acquired resolution: 0.6x0.6x1 mm^3; reconstructed resolution: 0.35x0.35x0.35 mm^3; slice orientation: coronal; repetition time/echo time: 7/3.5 ms; Flip angle: 55; acceleration factor: 1.2 feet-head direction; number of signal averages: 1; acquisition time: 4 min 30 sec.

Structural MRI of the Thoracolumbar Spine

Each subject underwent structural MRI of the thoracolumbar spine on a 3T MR scanner (Magnetom Prisma^{fit}, Siemens Healthineers) with 16-channel body and 32-channel spine array coils. Participants were positioned supine with arms at their side. Prior to MR image acquisition, shim boxes were applied to correct for magnetic field inhomogeneities. The standard MRI protocol comprised the following three pulse sequences, all used without gadolinium-based contrast agent administration: a) 2D sagittal T2-weighted turbo spin-echo (repetition time (TR), 3080 msec; echo time (TE), 98 msec; voxel size, 0.6×0.6×3 mm^3); b) 3D axial T2-weighted SPACE (Sampling Perfection with Application-optimized Contrasts using different flip angle Evolution) with ZOOMit (dynamic excitation pulses to achieve selective/zoomed field-of-view) software (TR, 2500 msec; TE, 106 msec; interpolated voxel size, 0.3×0.3×0.5 mm^3); and c) 3D coronal T2-weighted TrueFISP (True Fast Imaging with Steady state Precession) (TR, 6.04 msec; TE, 3.02 msec; interpolated voxel size, 0.3×0.3×0.6 mm^3). The total scan time was <25 min overall.

Detailed acquisition parameters for the three MR pulse sequences used to image the medullary cone and nerve roots of the participants' thoracolumbar spine:

Technical parameter	**T2-weighted turbo spin-echo**	**T2-weighted SPACE with ZOOMit**	**T2-weighted TrueFISP**
Plane	Sagittal	Axial	Coronal
No. of sections	21	160	80
Section thickness (mm)	3	0.5	0.6
Section gap (mm)	0.3	0	0
Field of view (mm)	290 × 333	300 × 105	250 × 250
Acquisition matrix	448 × 314	512 × 512	448 × 224
Voxel size (mm^3)	0.6 × 0.6 × 3	0.3 × 0.3 × 0.5*	0.3 × 0.3 × 0.6*
K-space sampling	Cartesian	Spiral	Cartesian
Phase-encoding direction	Head to feet	Anterior to posterior	Feet to head
Repetition time (ms)	4560	3080	6.04
Echo time (ms)	98	106	3.02
Turbo factor	19	270	N/A
No. of signal averages	2	1.4	1
Flip angle (degrees)	127	100	52
Bandwidth (Hz/pixel)	228	574	558
Acquisition time (min:sec)	2:41	10:11	6:55

* after interpolation

Spinal cord fMRI

We performed lumbosacral spinal cord functional magnetic imaging (fMRI) to obtain visualize the projectome of proprioceptive neurons innervating specific muscles. Muscle spindle afferents, which sense the length and change in length of the muscle wherein they are embedded, were recruited by passive muscle stretch (three participants) and muscle tendon vibrations (one participant). The fMRI pre-processing, processing and analysis pipeline were based on recent cervical spinal cord fMRI studies[2–6]. We tailored this pipeline to image the lumbar spinal cord.

fMRI data acquisition

Participants were comfortably installed in the scanner (Siemens Prisma 3 Tesla, Erlangen, Germany) in a supine position. Spine and body coils (Siemens, Erlangen, Germany) were used. The participants were instructed to relax, to remain still and to breathe normally. All three participants underwent at least one experimental recording, involving passive limb mobilization to stretch specific groups of muscles. Participants P3 was involved in an additional acquisition during which muscle tendon vibrations were applied to selected muscles (see below). Functional acquisitions were performed using a gradient-echo echo-planar sequence with a ZOOmit field-of-view imaging, with repetition time (TR) = 2.5 s, echo time (TE) = 34 ms, FOV = 48x144 mm, flip angle = 80°, in plane resolution = 1.1 mm x 1.1 mm, and slice thickness = 3 mm. 27 axial slices were acquired per volume. The first slice rostro caudally is placed slightly above the L1 segment. Manual shimming adjustments focused on the spinal cord were done to adjust field homogeneity. Physiological data (respiratory and cardiac signals) were directly acquired using MRI compatible photoplethysmography and respiratory belt (Siemens, Erlangen, Germany).

A T2-weighted high-resolution anatomical image (sequence SPACE with a resolution of 0.4 mm x 0.4 mm x 0.8 mm, TR = 1.5 s, TE = 135 ms) was also acquired for registration and normalization purposes.

Personalized hybrid computational models

Semi-automatic segmentation of anatomical tissues from MRI and CT data

Segmentation of MRI and CT data was performed using iSeg, a software developed by ZMT (www.zurichmedtech.com). We augmented this software with two plugins that accelerate the segmentation process. First, a Kalman-filter based plugin called *Root tracer* was implemented. *Root Tracer* utilizes the same algorithm as iSeg's *Auto-Tube Tracer* plugin to label the spinal roots semi-automatically. In each algorithm step, the current image slice is transformed into a label map which contains all identified roots. Each root is represented by a distinct label object. The plugin enables the user to manually correct missing or falsely identified spinal roots. The plugin then predicts the position of the successive roots in the consecutive slice by considering (a) the distance between the given root and all roots in the previous slice, (b) the difference in parameters between the given root and all roots in the previous slice (for more information on considered parameters see itk::ShapeLabelObject) and (c) a unique Kalman filter for each root that utilizes the position of all occurrences of the given root in the previous slices to predict its next position. The probability of root x from the current slice being root a from the previous slice is defined as:

$$P(x = a) = \frac{e^{-(w_d \times D_{x\to a} + w_p \times \Delta P_{x\to a} + w_k \times \Delta K_{x\to a})}}{\sum_i^N e^{-(w_d \times D_{x\to i} + w_p \times \Delta P_{x\to i} + w_k \times \Delta K_{x\to i})}}$$

Where $D_{x\to a}$ is the physical difference on the image between root x and a. $\Delta P_{x\to a}$ is the difference in parameters between root x and a. $\Delta K_{x\to a}$ is the difference between the Kalman filter's prediction between root x and a. W_d, w_p and w_k are user-defined weights relating to these parameters.

A second plugin, named *CT Auto-Bone,* enables the automated segmentation of vertebral bones from CT data. This plugin leverages a method based on enhancing the sheetness appearance of the cortical bone [25], i.e. the brighter CT pixel layer corresponding to bone boundaries. The sheetness measure is computed from the eigenvalues of the local Hessian (second derivatives of image intensities) and is used as the boundary term for an automatic graph-cut segmentation. The implementation uses the Graph Cut combinatorial optimization library (https://github.com/odanek/gc) and is available as a plugin in medical image segmentation tool set iSEG (https://github.com/ITISFoundation/osparc-iseg).

Generation of spinal cord 3D models

All relevant anatomical tissues were segmented in iSeg v 3.10.43.78. The procedure consisted of implementing the *CT Auto-Bone* plugin to segment the vertebral bone from the CT data. The space between the vertebral bodies was then filled with vertebral discs when possible, by means of thresholding, manual segmentation and interpolation. Similarly, the vertebral bone, cerebrospinal fluid and white matter were extracted from high-resolution MRI images. The *Root Tracer* plugin was applied to the same MRI images to identify the spinal roots. The epidural space was filled with another tissue named epidural fat by means of boolean subtraction between an enlarged cerebrospinal fluid and vertebral bone. The grey matter was placed to scale inside of the white matter, using contours generated from anatomical data[26].

The simulations were then implemented in Sim4Life[27]. Sim4Life is a multi-physics simulation platform with the capacity to model the physics, biology and physiology of living tissue and the interaction between neuromodulation technologies and living tissue. This simulation environment consists of detailed, parametrized anatomical models, image-based modelling functionality (segmentation, property maps...), a geometric modelling and meshing tool, a wide range of simulators (finite element method and others) and optimizers, a framework for the rapid development of high performance computing-enabled (parallelization, hardware acceleration) numerical solvers, a visualization toolkit-based visualization and postprocessing engine, a PYTHON scripting interface for customized applications, a coupling framework, neuronal solvers and more.

The segmented images were then imported in Sim4Life v6.2.0.4280 (ZMT. www.zurichmedtech.com) and transformed into a 3D model using the *Surface Extraction* tool. The coordinates of the spinal roots were extracted as x-y-z coordinates. We developed a custom-made algorithm to generate a continuum of rootlets for each spinal root. This algorithm was based on the assumptions that each rootlet has a fixed diameter and that the lower thoracic and lumbosacral spinal cord exhibit a continuum of rootlets with only minor empty spaces in between the roots along the rostrocaudal direction. Concretely, the centerlines of two roots were extracted and the 3D coordinates at the entry point into the white matter were used to interpolate the trajectories of the rootlets. The number of rootlets was determined by the distance between the entry-points under the assumption that each rootlet has a fixed diameter. Rootlet diameters were assigned based on anatomical observations[28]. Elliptical cross-sections were placed along the trajectories with their normal vector parallel to the tangent vector of the trajectory. Finally, the contours that defined the rootlets were imported in Sim4Life and lofted together using the *SkinWire* function.

Model of the paddle leads

We created a model of the new paddle lead and of the Specify 5-6-5. These models were composed of 3D orthopes with rounded edges to depict the electrodes. The electrodes were placed inside another 3D orthope with rounded edges that modelled the paddle lead. The models of the paddle leads were positioned at distinct locations within the epidural space to study the interactions between the location of the stimulation and the recruitment of afferent fibers.

Finite element models

Due to the variability in the topological organization of the spinal cord amongst the studied human population, we discretized the models as voxels using the robust rectilinear (structured) gridding engine provided by Sim4Life. Region-specific grid resolution thresholds were imposed: maximum 2 mm for vertebral bone and discs, 1 mm for the epidural fat and cerebrospinal fluid, 0.6 mm for the paddle lead of the spinal cord stimulator, 0.3 mm for the grey and white matter, as well as any electrodes and 0.1 mm for the rootlets. The entire model was submerged in a large conducting material to simulate the human body. This material is referred to as saline conductor (-10 mm grid resolution threshold). We applied conductivity maps for each tissue. Conductivity values were taken from a previously published study[29]. Similar to previous studies, we did not include the thin dura mater in our model[30]. To model the anisotropic conductivity of the white matter and rootlets, we expanded the capability of Sim4Life to enable the automatic calculation of anisotropic and inhomogeneous conductivity maps from helper simulations. These helpers solve the Laplace Equation ($\Delta V = 0$) with the following Dirichlet and Neumann boundary conditions: $V(\delta\Omega_{rostral}) = 1$ at the rostral surface of the white matter, $V(\delta\Omega_{caudal}) = 0$ at the caudal end of each rootlet and the inferior tip of the white matter, and isolating ($|\nabla V| = 0$). We solved the electro-quasistatic approximation of the Maxwell equations using the Sim4Life solver ($\nabla\sigma\nabla\varphi = 0$, with σ the conductivity and φ the permittivity), while assigning a constant σ throughout the computational domain, which comprised white matter and rootlets. The resulting E-fields (proportional to the potential gradients), were then used to define the local orientation of the principal conduction components of the anisotropic tissue conductivity. The tensor was computed according to the following equation:

$$(\sigma(x) = \sigma_{longitudinal} \times P(x) + \sigma_{transversal} \times \left(I_3 - P(x)\right), \text{ where },P(x) = E(X) \otimes (\tfrac{E(X)}{E(X)^2}).$$

Simulation of EES in the Model

The electrical potential induced by EES was obtained by solving the electro-quasistatic approximation of the Maxwell equations. The corresponding simulation has already been predefined and is available in Sim4Life. A Dirichlet Boundary condition of $V(\delta\Omega_{electrode}) = 1V$ simulating a biphasic stimulation pulse of 500 µs duration was applied at the active electrode site ($\delta\Omega_{electrode}$) to model the stimulation commonly occurring throughout this study. Dirichlet boundary conditions of $V(\delta\Omega_{saline}) = -1V$ were set at the location of a return electrode within the saline conductor to simulate the position of the implantable pulse generator. Von Neumann conditions with $\frac{\partial V}{\partial x} = 0$ were applied at the outermost surface of the saline conductor. Convergence tolerance were set to the predefined value high.

Modeling and recruitment of nerve fibers

We used the integrated NEURON 6.0.0.3176[31] solver of Sim4Life to develop a computational model of group Aα-, Aβ-, Aδ- and C-fibers that we positioned within the dorsal roots, and of α-motor axons that we positioned in the ventral roots. Fifty fibers per fiber population were simulated for each spinal cord segment. The trajectories of the fibers were automatically generated, by uniformly distributing 50 points $P_{i,n}$ in each Contour C_n and connecting those that have the same index i. To ensure that nerve fibers remain similarly positioned relative to each other inside each rootlet (i.e., the fibers are not meandering), we use a single set of weights $w_{i,l}$ according to:

$$P_{i,n} = \sum_{l=1}^{N} w_{i,l} \times \begin{pmatrix} X_{ln} \\ Y_{ln} \\ Z_{ln} \end{pmatrix}$$

where $(X_{ln}, Y_{ln}, Z_{ln},)$are the coordinates of the N points composing C_n. The weights w_l are sampled uniformly at random in the unit simplex. This was possible as the C_n were defined with similar topologies, namely that they posses the same number of points N with equal indexes which are isomorphic. Finally, the trajectories of these splines were interpolated to smooth their trajectories and imported in Sim4Life. Compartmental cable models were then applied to these trajectories. We designed Sensory MRG model[32] that we integrated into Sim4Life to simulate Aα- and Aβ-fibers with arbitrary diameters. We also integrated Motor MRG models[32] with arbitrary diameters for the α-motor axons. Finally, wee simulated Aδ-fibers with Sweeney Models[33] and C-fibers with Sundt-Models[34]. Diameters of nerve fibers were stochastically assigned according to log-norm distributions with the following parameters: Aα: μ = 16.5 μm, σ = 2 μm; Aβ: μ = 10,5 μm, σ = 2 μm; Aδ: μ = 3 μm, σ = 1 μm; C = μ = 0.85 μm, σ = 0.5 μm; MN: μ = 11.52 μm, σ = 0.07 μm. For each amplitude of EES, we calculated the recruitment curve of each population of fibers for increasing EES amplitudes.

Dorsal root selectivity index

For a given electrode configuration and EES amplitude, computational simulations yielded the percentage of fibers activated in each dorsal root. We derived a root selectivity index $SI_{computational}(r_i, I)$ for each root r_i and each stimulation amplitude I:

$$SI_{computational}(r_i, I) = \frac{A_{r_i}(I)}{1 + \sum_{other\ ipsilateral\ roots} A_{r_j}(I)} . f_+\left(\frac{A_{r_i}(I) - A_{r_{contralateral(i)}}(I)}{A_{r_i}(I) + A_{r_{contralateral(i)}}(I)}\right)$$

where $A_{r_i}(I)$ represents the percentage of fibers activated in root r_i, $r_{contralateral(i)}$ is the root contratateral to root r_i , and $f_+(x) = \begin{cases} x\ if\ x > 0 \\ 0\ if\ x \leq 0 \end{cases}$.

The first term of this selectivity index represents the rostro-caudal ipsilateral root selectivity, while the second term indicates the medio-lateral selectivity and penalizes configurations that activate the root contralateral to the targeted one. If the contralateral root is more activated than the targeted root, the selectivity index is equal to 0. If only the targeted root is recruited, the selectivity equals 1. This selectivity index was calculated for a range of stimulation amplitudes and the maximum was taken to characterize the overall selectivity of each electrode configuration.

Preoperative placement optimization

To optimize the intraoperative placement of the paddle leads, we performed simulations based on the personalized model of each participant. We manually placed a model of the new paddle lead and Specify 5-6-5 in the epidural space. Since simulations revealed that Aα fibers are nearly all activated before the recruitment of the other fiber populations (**Fig. 1**), we only considered Aα-fibers in the dorsal rootlets, thus allowing to optimize computational resources. We computed the electric potential scaling required to recruit each fiber. We then calculated the percentage of fibers recruited within each spinal segment at each electric potential scaling I and interpolated this recruitment profile to 10’000 datapoints over the entire electric potential scaling required to activate each fiber in the model with each electrode at each position of the paddle lead. We then elaborated transformation matrices to translate this afferent recruitment profile to an estimation of the recruitment of motor neurons and thus muscle activity $A_j(I)$, where j denoted the muscle. Two transformation matrices were used. First, we built a transformation matrix for each patient based on the projectome of proprioceptive neurons from key leg muscles identified from fMRI acquisitions. Second, we built a generic transformation matrix based on the distribution of myotomes measured electrophysiologically in a large population of patients undergoing surgery[35]. These matrices can be found below:

Patient P1	Iliopsoas	Rectus Femoris/ Vastus Lateralis	Semi-Tendinosis	Tibialis Anterior	Gastrocnemius Medialis/ Soleus
L1	0	0	0	0	0
L2	1	0	0	0	0
L3	0	1	0.07	0	0
L4	0	0	0.23	0	0
L5	0	0	0.4	1	0
S1	0	0	0.3	0	0.5
S2	0	0	0	0	0.5

Patient P2	Iliopsoas	Rectus Femoris/ Vastus Lateralis	Semi-tendinosis	Tibialis Anterior	Gastrocnemius Medialis/ Soleus
L1	0.7	0.1	0	0	0
L2	0.3	0.6	0	0	0
L3	0	0.3	0.07	0	0
L4	0	0	0.23	0.4	0
L5	0	0	0.4	0.5	0.4
S1	0	0	0.3	0.1	0.5
S2	0	0	0	0	0.1

Patient P3	Iliopsoas	Rectus Femoris/ Vastus Lateralis	Semi-tendinosis	Tibialis Anterior	Gastrocnemius Medialis/ Soleus
L1	0.5	0	0	0	0
L2	0.5	0	0	0	0
L3	0	1	0	0	0
L4	0	0	0	0	0.5
L5	0	0	1	0	0.5
S1	0	0	0	1	0
S2	0	0	0	0	0

Literature	Iliopsoas	Rectus Femoris/	Semi-Tendinosus	Tibialis Anterior	Gastrocnemius Medialis/ Soleus

		Vastus Lateralis			
L1	0.45	0.12	0	0	0
L2	0.3	0.27	0	0	0
L3	0.17	0.37	0.07	0.04	0.01
L4	0.06	0.24	0.23	0.34	0.08
L5	0.01	0	0.4	0.43	0.17
S1	0.01	0	0.3	0.19	0.38
S2	0	0	0	0	0.36

To identify the optimal placement of the paddle lead, we computed a selectivity index $SI_{functionality}(g_i\ I)$ that quantified the performance of an electrode to target a muscle group g_i with respect to non-targeted muscles. This selectivity index contains two terms, one indicating the selectivity on the targeted side, and one indicating the mediolateral selectivity for the targeted side s_i:

$$SI_{functionality}(g_i, I) = SI_{targeted\ musles}(g_i, I)\ .SI_{left\ vs\ right}(s_i, I)$$

$$\begin{cases} SI_{targeted\ muscles}(g_i, I) = f_+\left(\dfrac{\sum_{muscles\ in\ g_i}\omega_{i,j}\ .\log\left(1+A_j(I)\right)}{\log 2}\right) \\ SI_{left\ vs\ right}(s_i, I) = f_+\left(\dfrac{max_{ipsilateral(s_i)}\left(A_j(I)\right) - max_{contralateral(s_i)}\left(A_j(I)\right)}{max_{ipsilateral(s_i)}\left(A_j(I)\right) + max_{contralateral(s_i)}\left(A_j(I)\right)}\right) \\ f_+(x) = \begin{cases} x\ if\ x > 0 \\ 0\ if\ x \leq 0 \end{cases} \end{cases}$$

where $A_j(I)$ represents the normalized activity of the muscle *j* in response to EES delivered at the amplitude *I*. $\omega_{i,j}$ is a weight associated with the muscle *j* for the targeted muscle group g_i and is summarized in the table below. For each targeted muscle group, weights of agonists (respectively antagonists) are positive (respectively negative), and the sum of weights over agonists (respectively antagonists) is equal to 1 (respectively -1). These weights were chosen empirically to capture the respective contributions of each muscle in the targeted muscle group.

We then chose the maximum selectivity index for each targeted muscle group among all selectivity indices computed for each electrode in a given position of the paddle lead. We then calculated the average of these selectivity indices for each targeted muscle group at each location of the paddle lead, while penalizing the performance when a targeted muscle group was theoretically not reachable:

$$SI_{average} = \frac{1}{4}\sum_i SI_i$$

Where $SI_i = \begin{Bmatrix} SI_{functionality}\ of\ functionality\ i \\ 0.5 \times SI_{functionality}\ of\ functionality\ i \end{Bmatrix}$

and $i \in \{left\ hip\ flexion, right\ hip\ flexion, left\ ankle\ extension, right\ ankle\ extension\}$.

	Iliopsoas	Rectus Femoris/ Vastus Lateralis	Semi-Tendinosus	Tibialis Anterior	Gastrocnemius Medialis/ Soleus
Hip flexion (L1)	0.8	0.2	-1	-	-
Ankle extension (S1)	-	-	-	-1	1

Lower limb selectivity index calculated with experimental data

To quantify the performance of the paddle leads to target specific dorsal roots, we computed a selectivity index $SI_{experimental}(g_i\ I)$ for each targeted muscle group g_i and EES amplitude I. This selectivity index contains two terms, one indicating the selectivity on the targeted side, and one indicating the mediolateral selectivity for the targeted side s_i:

$$SI_{experimental}(g_i, I) = SI_{targeted\ musles}(g_i, I)\ .SI_{left\ vs\ right}(s_i, I)$$

$$\begin{cases} SI_{targeted\ muscles}(g_i, I) = f_+\left(\dfrac{\sum_{muscles\ in\ g_i} \omega_{i,j}\ .\log\left(1 + A_j(I)\right)}{\log 2}\right) \\ SI_{left\ vs\ right}(s_i, I) = f_+\left(\dfrac{max_{ipsilateral(s_i)}\left(A_j(I)\right) - max_{contralateral(s_i)}\left(A_j(I)\right)}{max_{ipsilateral(s_i)}\left(A_j(I)\right) + max_{contralateral(s_i)}\left(A_j(I)\right)}\right) \\ f_+(x) = \begin{cases} x\ if\ x > 0 \\ 0\ if\ x \leq 0 \end{cases} \end{cases}$$

where $A_j(I)$ represents the normalized muscle response when delivering a single pulse of EES at the amplitude I. $\omega_{i,j}$ is a weight associated with the muscle j for the targeted muscle group g_i.. For each targeted muscle group, weights of agonists (respectively antagonists) are positive (respectively negative), and the sum of weights over agonists (respectively antagonists) is equal to 1 (respectively -1). These weights were chosen to capture the respective contributions of each muscle in the targeted hotspot:

	Iliopsoas	Rectus Femoris	Vastus Lateralis	Semi-Tendinosus	Tibialis Anterior	Gastrocnemius Medialis	Soleus
Hip flexion (L1)	0.8	0.2	-	-1	-	-	-
Ankle extension (S1)	-	-	-	-	-1	0.2	0.8
Weight Acceptance	-0.3	0.2	0.8-	-0.5			-0.2
Whole Leg Flexion	0.4	-	-0.45		0.6	-0.1	-0.45
Propulsion	-0.5			0.5	-0.5	0.1	0.4

We then chose the maximum selectivity index for each targeted dorsal root among all selectivity indices computed for each tested electrode at a given position of the paddle lead.

We then calculated the average of these selectivity indices for targeted dorsal root at each lead location:

$$SI_{average} = \frac{1}{4}\sum_{i} SI_i$$

Where $SI_i = \begin{Bmatrix} SI_{functionality}\ of\ functionality\ i \\ 0.5 \times SI_{functionality}\ of\ functionality\ i \end{Bmatrix}$ and $i \in \{left\ hip\ flexion, right\ hip\ flexion, left\ ankle\ extension, right\ ankle\ extension\}$.

Trunk selectivity index

To quantify the relative selectivity of trunk recruitment compared to the recruitment of lower limb muscles, the lower-limb selectivity index was adapted with the following weights:

	Upper Abdominals	Obliques	Quadratus Lomborum	Iliopsoas	Adductors	Rectus Femoris
Trunk	0.33	0.33	0.33	-0.33	-0.33	-0.33

REFERENCES

1. Kirshblum, S. & Waring, W. Updates for the International Standards for Neurological Classification of Spinal Cord Injury. *Phys Med Rehabil Cli* **25**, 505–517 (2014).

2. Weber, K. A. *et al.* Assessing the spatial distribution of cervical spinal cord activity during tactile stimulation of the upper extremity in humans with functional magnetic resonance imaging. *Neuroimage* **217**, 116905 (2020).

3. Kinany, N., Pirondini, E., Micera, S. & Ville, D. V. D. Dynamic Functional Connectivity of Resting-State Spinal Cord fMRI Reveals Fine-Grained Intrinsic Architecture. *Neuron* **108**, 424-435.e4 (2020).

4. Kinany, N. *et al.* Functional imaging of rostrocaudal spinal activity during upper limb motor tasks. *Neuroimage* **200**, 590–600 (2019).

5. Weber, K. A., Chen, Y., Wang, X., Kahnt, T. & Parrish, T. B. Functional magnetic resonance imaging of the cervical spinal cord during thermal stimulation across consecutive runs. *Neuroimage* **143**, 267–279 (2016).

6. Weber, K. A., Chen, Y., Wang, X., Kahnt, T. & Parrish, T. B. Lateralization of cervical spinal cord activity during an isometric upper extremity motor task with functional magnetic resonance imaging. *Neuroimage* **125**, 233–243 (2016).

7. Roll, J. P. & Vedel, J. P. Kinaesthetic role of muscle afferents in man, studied by tendon vibration and microneurography. *Exp Brain Res* **47**, 177–190 (1982).

8. Landelle, C., Ahmadi, A. E. & Kavounoudias, A. Age-Related Impairment of Hand Movement Perception Based on Muscle Proprioception and Touch. *Neuroscience* **381**, 91–104 (2018).

9. Kavounoudias, A. *et al.* Proprio-tactile integration for kinesthetic perception: An fMRI study. *Neuropsychologia* **46**, 567–575 (2008).

10. Jenkinson, M., Beckmann, C. F., Behrens, T. E. J., Woolrich, M. W. & Smith, S. M. FSL. *Neuroimage* **62**, 782–790 (2012).

11. Leener, B. D. *et al.* SCT: Spinal Cord Toolbox, an open-source software for processing spinal cord MRI data. *Neuroimage* **145**, 24–43 (2017).

12. Jenkinson, M., Bannister, P., Brady, M. & Smith, S. Improved Optimization for the Robust and Accurate Linear Registration and Motion Correction of Brain Images. *Neuroimage* **17**, 825–841 (2002).

13. Gros, C. *et al.* Automatic spinal cord localization, robust to MRI contrasts using global curve optimization. *Med Image Anal* **44**, 215–227 (2018).

14. K., W., C.Y., I., X., W. & T., P. Choice of motion correction method affects spinal cord fMRI results. in *20th Annual Meeting of the Organization for Human Brain Mapping* (2014).

15. Cohen-Adad, J. *et al.* Venous effect in spinal cord fMRI: insights from intrinsic optical imaging and laser speckle. *Neuroimage* **47**, S186 (2009).

16. Power, J. D. *et al.* Methods to detect, characterize, and remove motion artifact in resting state fMRI. *Neuroimage* **84**, 320–341 (2014).

17. Gros, C. *et al.* Automatic segmentation of the spinal cord and intramedullary multiple sclerosis lesions with convolutional neural networks. *Neuroimage* **184**, 901–915 (2019).

18. Eippert, F., Kong, Y., Jenkinson, M., Tracey, I. & Brooks, J. C. W. Denoising spinal cord fMRI data: Approaches to acquisition and analysis. *Neuroimage* **154**, 255–266 (2017).

19. Brooks, J. C. W. *et al.* Physiological noise modelling for spinal functional magnetic resonance imaging studies. *Neuroimage* **39**, 680–692 (2008).

20. Kong, Y., Jenkinson, M., Andersson, J., Tracey, I. & Brooks, J. C. W. Assessment of physiological noise modelling methods for functional imaging of the spinal cord. *Neuroimage* **60**, 1538–1549 (2012).

21. Behzadi, Y., Restom, K., Liau, J. & Liu, T. T. A component based noise correction method (CompCor) for BOLD and perfusion based fMRI. *Neuroimage* **37**, 90–101 (2007).

22. Kasper, L. *et al.* The PhysIO Toolbox for Modeling Physiological Noise in fMRI Data. *J Neurosci Meth* **276**, 56–72 (2017).

23. Woolrich, M. W., Ripley, B. D., Brady, M. & Smith, S. M. Temporal Autocorrelation in Univariate Linear Modeling of FMRI Data. *Neuroimage* **14**, 1370–1386 (2001).

24. Woolrich, M. W., Behrens, T. E. J. & Smith, S. M. Constrained linear basis sets for HRF modelling using Variational Bayes. *Neuroimage* **21**, 1748–1761 (2004).

25. Krcah, M., Szekely, G. & Blanc, R. Fully Automatic and Fast Segmentation of the Femur Bone from 3D-CT Images with No Shape Prior. *2011 Ieee Int Symposium Biomed Imaging Nano Macro* 2087–2090 (2011) doi:10.1109/isbi.2011.5872823.

26. Akkın, S. M. Atlas of the Spinal Cord of the Rat, Mouse, Marmoset, Rhesus and Human by Gulgun Sengul, Charles Watson, Ikuko Tanaka and George Paxinos. *Anat* **7**, 68–68 (2015).

27. Neufeld, E., Szczerba, D., Chavannes, N. & Kuster, N. A novel medical image data-based multi-physics simulation platform for computational life sciences. *Interface Focus* **3**, 20120058 (2013).

28. Liu, Y., Zhou, X., Ma, J., Ge, Y. & Cao, X. The diameters and number of nerve fibers in spinal nerve roots. *J Spinal Cord Medicine* **38**, 532–537 (2014).

29. Capogrosso, M. *et al.* A Computational Model for Epidural Electrical Stimulation of Spinal Sensorimotor Circuits. *J Neurosci* **33**, 19326–19340 (2013).

30. Ladenbauer, J., Minassian, K., Hofstoetter, U. S., Dimitrijevic, M. R. & Rattay, F. Stimulation of the Human Lumbar Spinal Cord with Implanted and Surface Electrodes: A Computer Simulation Study. *Ieee T Neur Sys Reh* **18**, 637–645 (2010).

31. Hines, M. L. & Carnevale, N. T. Neuron: A Tool for Neuroscientists. *Neurosci* **7**, 123–135 (2001).

32. Gaines, J. L., Finn, K. E., Slopsema, J. P., Heyboer, L. A. & Polasek, K. H. A model of motor and sensory axon activation in the median nerve using surface electrical stimulation. *J Comput Neurosci* **45**, 29–43 (2018).

33. D., S., J.T., M. & D., D. Modeling of mammalian myelinated nerve for functional neuromuscular stimulation. in *IEEE/Engineering in Medicine and Biology Society Annual Conference* (IEEE, 1987).

34. Sundt, D., Gamper, N. & Jaffe, D. B. Spike propagation through the dorsal root ganglia in an unmyelinated sensory neuron: a modeling study. *J Neurophysiol* **114**, 3140–3153 (2015).

35. Schirmer, C. M. *et al.* Heuristic map of myotomal innervation in humans using direct intraoperative nerve root stimulation: Clinical article. *J Neurosurg Spine* **15**, 64–70 (2011).

36. Wagner, F. B. *et al.* Targeted neurotechnology restores walking in humans with spinal cord injury. *Nature* **563**, 65–71 (2018).

37. Gomez-Perez, S. L. *et al.* Measuring Abdominal Circumference and Skeletal Muscle From a Single Cross-Sectional Computed Tomography Image. *Jpen-parenter Enter* **40**, 308–318 (2016)